Top quark mass measurement in the lepton plus jets channel using a modified matrix element method

T. Aaltonen,[24] J. Adelman,[14] T. Akimoto,[56] B. Álvarez González,[12,r] S. Amerio,[44a,44b] D. Amidei,[35] A. Anastassov,[39] A. Annovi,[20] J. Antos,[15] G. Apollinari,[18] A. Apresyan,[49] T. Arisawa,[58] A. Artikov,[16] W. Ashmanskas,[18] A. Attal,[4] A. Aurisano,[54] F. Azfar,[43] P. Azzurri,[47a,47d] W. Badgett,[18] A. Barbaro-Galtieri,[29] V. E. Barnes,[49] B. A. Barnett,[26] V. Bartsch,[31] G. Bauer,[33] P.-H. Beauchemin,[34] F. Bedeschi,[47a] D. Beecher,[31] S. Behari,[26] G. Bellettini,[47a,47b] J. Bellinger,[60] D. Benjamin,[17] A. Beretvas,[18] J. Beringer,[29] A. Bhatti,[51] M. Binkley,[18] D. Bisello,[44a,44b] I. Bizjak,[31,w] R. E. Blair,[2] C. Blocker,[7] B. Blumenfeld,[26] A. Bocci,[17] A. Bodek,[50] V. Boisvert,[50] G. Bolla,[49] D. Bortoletto,[49] J. Boudreau,[48] A. Boveia,[11] B. Brau,[11,b] A. Bridgeman,[25] L. Brigliadori,[44a] C. Bromberg,[36] E. Brubaker,[14] J. Budagov,[16] H. S. Budd,[50] S. Budd,[25] S. Burke,[18] K. Burkett,[18] G. Busetto,[44a,44b] P. Bussey,[22] A. Buzatu,[34] K. L. Byrum,[2] S. Cabrera,[17,t] C. Calancha,[32] M. Campanelli,[36] M. Campbell,[35] F. Canelli,[14,18] A. Canepa,[46] B. Carls,[25] D. Carlsmith,[60] R. Carosi,[47a] S. Carrillo,[19,m] S. Carron,[34] B. Casal,[12] M. Casarsa,[18] A. Castro,[6a,6b] P. Catastini,[47a,47c] D. Cauz,[55a,55b] V. Cavaliere,[47a,47c] M. Cavalli-Sforza,[4] A. Cerri,[29] L. Cerrito,[31,n] S. H. Chang,[28] Y. C. Chen,[1] M. Chertok,[8] G. Chiarelli,[47a] G. Chlachidze,[18] F. Chlebana,[18] K. Cho,[28] D. Chokheli,[16] J. P. Chou,[23] G. Choudalakis,[33] S. H. Chuang,[53] K. Chung,[13] W. H. Chung,[60] Y. S. Chung,[50] T. Chwalek,[27] C. I. Ciobanu,[45] M. A. Ciocci,[47a,47c] A. Clark,[21] D. Clark,[7] G. Compostella,[44a] M. E. Convery,[18] J. Conway,[8] M. Cordelli,[20] G. Cortiana,[44a,44b] C. A. Cox,[8] D. J. Cox,[8] F. Crescioli,[47a,47b] C. Cuenca Almenar,[8,t] J. Cuevas,[12,r] R. Culbertson,[18] J. C. Cully,[35] D. Dagenhart,[18] M. Datta,[18] T. Davies,[22] P. de Barbaro,[50] S. De Cecco,[52a] A. Deisher,[29] G. De Lorenzo,[4] M. Dell'Orso,[47a,47b] C. Deluca,[4] L. Demortier,[51] J. Deng,[17] M. Deninno,[6a] P. F. Derwent,[18] G. P. di Giovanni,[45] C. Dionisi,[52a,52b] B. Di Ruzza,[55a,55b] J. R. Dittmann,[5] M. D'Onofrio,[4] S. Donati,[47a,47b] P. Dong,[9] J. Donini,[44a] T. Dorigo,[44a] S. Dube,[53] J. Efron,[40] A. Elagin,[54] R. Erbacher,[8] D. Errede,[25] S. Errede,[25] R. Eusebi,[18] H. C. Fang,[29] S. Farrington,[43] W. T. Fedorko,[14] R. G. Feild,[61] M. Feindt,[27] J. P. Fernandez,[32] C. Ferrazza,[47a,47d] R. Field,[19] G. Flanagan,[49] R. Forrest,[8] M. J. Frank,[5] M. Franklin,[23] J. C. Freeman,[18] I. Furic,[19] M. Gallinaro,[52a] J. Galyardt,[13] F. Garberson,[11] J. E. Garcia,[21] A. F. Garfinkel,[49] K. Genser,[18] H. Gerberich,[25] D. Gerdes,[35] A. Gessler,[27] S. Giagu,[52a,52b] V. Giakoumopoulou,[3] P. Giannetti,[47a] K. Gibson,[48] J. L. Gimmell,[50] C. M. Ginsburg,[18] N. Giokaris,[3] M. Giordani,[55a,55b] P. Giromini,[20] M. Giunta,[47a,47b] G. Giurgiu,[26] V. Glagolev,[16] D. Glenzinski,[18] M. Gold,[38] N. Goldschmidt,[19] A. Golossanov,[18] G. Gomez,[12] G. Gomez-Ceballos,[33] M. Goncharov,[33] O. González,[32] I. Gorelov,[38] A. T. Goshaw,[17] K. Goulianos,[51] A. Gresele,[44a,44b] S. Grinstein,[23] C. Grosso-Pilcher,[14] R. C. Group,[18] U. Grundler,[25] J. Guimaraes da Costa,[23] Z. Gunay-Unalan,[36] C. Haber,[29] K. Hahn,[33] S. R. Hahn,[18] E. Halkiadakis,[53] B.-Y. Han,[50] J. Y. Han,[50] F. Happacher,[20] K. Hara,[56] D. Hare,[53] M. Hare,[57] S. Harper,[43] R. F. Harr,[59] R. M. Harris,[18] M. Hartz,[48] K. Hatakeyama,[51] C. Hays,[43] M. Heck,[27] A. Heijboer,[46] J. Heinrich,[46] C. Henderson,[33] M. Herndon,[60] J. Heuser,[27] S. Hewamanage,[5] D. Hidas,[17] C. S. Hill,[11,c] D. Hirschbuehl,[27] A. Hocker,[18] S. Hou,[1] M. Houlden,[30] S.-C. Hsu,[29] B. T. Huffman,[43] R. E. Hughes,[40] U. Husemann,[61] M. Hussein,[36] J. Huston,[36] J. Incandela,[11] G. Introzzi,[47a] M. Iori,[52a,52b] A. Ivanov,[8] E. James,[18] D. Jang,[13] B. Jayatilaka,[17] E. J. Jeon,[28] M. K. Jha,[6a] S. Jindariani,[18] W. Johnson,[8] M. Jones,[49] K. K. Joo,[28] S. Y. Jun,[13] J. E. Jung,[28] T. R. Junk,[18] T. Kamon,[54] D. Kar,[19] P. E. Karchin,[59] Y. Kato,[42] R. Kephart,[18] J. Keung,[46] V. Khotilovich,[54] B. Kilminster,[18] D. H. Kim,[28] H. S. Kim,[28] H. W. Kim,[28] J. E. Kim,[28] M. J. Kim,[20] S. B. Kim,[28] S. H. Kim,[56] Y. K. Kim,[14] N. Kimura,[56] L. Kirsch,[7] S. Klimenko,[19] B. Knuteson,[33] B. R. Ko,[17] K. Kondo,[58] D. J. Kong,[28] J. Konigsberg,[19] A. Korytov,[19] A. V. Kotwal,[17] M. Kreps,[27] J. Kroll,[46] D. Krop,[14] N. Krumnack,[5] M. Kruse,[17] V. Krutelyov,[11] T. Kubo,[56] T. Kuhr,[27] N. P. Kulkarni,[59] M. Kurata,[56] S. Kwang,[14] A. T. Laasanen,[49] S. Lami,[47a] S. Lammel,[18] M. Lancaster,[31] R. L. Lander,[8] K. Lannon,[40,q] A. Lath,[53] G. Latino,[47a,47c] I. Lazzizzera,[44a,44b] T. LeCompte,[2] E. Lee,[54] H. S. Lee,[14] S. W. Lee,[54,s] S. Leone,[47a] J. D. Lewis,[18] C.-S. Lin,[29] J. Linacre,[43] M. Lindgren,[18] E. Lipeles,[46] A. Lister,[8] D. O. Litvintsev,[18] C. Liu,[48] T. Liu,[18] N. S. Lockyer,[46] A. Loginov,[61] M. Loreti,[44a,44b] L. Lovas,[15] D. Lucchesi,[44a,44b] C. Luci,[52a,52b] J. Lueck,[27] P. Lujan,[29] P. Lukens,[18] G. Lungu,[51] L. Lyons,[43] J. Lys,[29] R. Lysak,[15] D. MacQueen,[34] R. Madrak,[18] K. Maeshima,[18] K. Makhoul,[33] T. Maki,[24] P. Maksimovic,[26] S. Malde,[43] S. Malik,[31] G. Manca,[30,f] A. Manousakis-Katsikakis,[3] F. Margaroli,[49] C. Marino,[27] C. P. Marino,[25] A. Martin,[61] V. Martin,[22,l] M. Martínez,[4] R. Martínez-Ballarín,[32] T. Maruyama,[56] P. Mastrandrea,[52a] T. Masubuchi,[56] M. Mathis,[26] M. E. Mattson,[59] P. Mazzanti,[6a] K. S. McFarland,[50] P. McIntyre,[54] R. McNulty,[30,k] A. Mehta,[30] P. Mehtala,[24] A. Menzione,[47a] P. Merkel,[49] C. Mesropian,[51] T. Miao,[18] N. Miladinovic,[7] R. Miller,[36] C. Mills,[23] M. Milnik,[27] A. Mitra,[1] G. Mitselmakher,[19] H. Miyake,[56] N. Moggi,[6a] C. S. Moon,[28] R. Moore,[18] M. J. Morello,[47a,47b] J. Morlock,[27] P. Movilla Fernandez,[18] J. Mülmenstädt,[29] A. Mukherjee,[18] Th. Muller,[27] R. Mumford,[26] P. Murat,[18] M. Mussini,[6a,6b] J. Nachtman,[18] Y. Nagai,[56] A. Nagano,[56] J. Naganoma,[56] K. Nakamura,[56] I. Nakano,[41] A. Napier,[57] V. Necula,[17] J. Nett,[60] C. Neu,[46,u]

M. S. Neubauer,[25] S. Neubauer,[27] J. Nielsen,[29,h] L. Nodulman,[2] M. Norman,[10] O. Norniella,[25] E. Nurse,[31] L. Oakes,[43] S. H. Oh,[17] Y. D. Oh,[28] I. Oksuzian,[19] T. Okusawa,[42] R. Orava,[24] K. Osterberg,[24] S. Pagan Griso,[44a,44b] E. Palencia,[18] V. Papadimitriou,[18] A. Papaikonomou,[27] A. A. Paramonov,[14] B. Parks,[40] S. Pashapour,[34] J. Patrick,[18] G. Pauletta,[55a,55b] M. Paulini,[13] C. Paus,[33] T. Peiffer,[27] D. E. Pellett,[8] A. Penzo,[55a] T. J. Phillips,[17] G. Piacentino,[47a] E. Pianori,[46] L. Pinera,[19] K. Pitts,[25] C. Plager,[9] L. Pondrom,[60] O. Poukhov,[16,a] N. Pounder,[43] F. Prakoshyn,[16] A. Pronko,[18] J. Proudfoot,[2] F. Ptohos,[18,j] E. Pueschel,[13] G. Punzi,[47a,47b] J. Pursley,[60] J. Rademacker,[43,d] A. Rahaman,[48] V. Ramakrishnan,[60] N. Ranjan,[49] I. Redondo,[32] P. Renton,[43] M. Renz,[27] M. Rescigno,[52a] S. Richter,[27] F. Rimondi,[6a,6b] L. Ristori,[47a] A. Robson,[22] T. Rodrigo,[12] T. Rodriguez,[46] E. Rogers,[25] S. Rolli,[57] R. Roser,[18] M. Rossi,[55a] R. Rossin,[11] P. Roy,[34] A. Ruiz,[12] J. Russ,[13] V. Rusu,[18] H. Saarikko,[24] A. Safonov,[54] W. K. Sakumoto,[50] O. Saltó,[4] L. Santi,[55a,55b] S. Sarkar,[52a,52b] L. Sartori,[47a] K. Sato,[18] A. Savoy-Navarro,[45] P. Schlabach,[18] A. Schmidt,[27] E. E. Schmidt,[18] M. A. Schmidt,[14] M. P. Schmidt,[61,a] M. Schmitt,[39] T. Schwarz,[8] L. Scodellaro,[12] A. Scribano,[47a,47c] F. Scuri,[47a] A. Sedov,[49] S. Seidel,[38] Y. Seiya,[42] A. Semenov,[16] L. Sexton-Kennedy,[18] F. Sforza,[47a] A. Sfyrla,[25] S. Z. Shalhout,[59] T. Shears,[30] P. F. Shepard,[48] M. Shimojima,[56,p] S. Shiraishi,[14] M. Shochet,[14] Y. Shon,[60] I. Shreyber,[37] A. Sidoti,[47a] J. Siegrist,[29] P. Sinervo,[34] A. Sisakyan,[16] A. J. Slaughter,[18] J. Slaunwhite,[40] K. Sliwa,[57] J. R. Smith,[8] F. D. Snider,[18] R. Snihur,[34] A. Soha,[8] S. Somalwar,[53] V. Sorin,[36] J. Spalding,[18] T. Spreitzer,[34] P. Squillacioti,[47a,47c] M. Stanitzki,[61] R. St. Denis,[22] B. Stelzer,[34] O. Stelzer-Chilton,[34] D. Stentz,[39] J. Strologas,[38] G. L. Strycker,[35] D. Stuart,[11] J. S. Suh,[28] A. Sukhanov,[19] I. Suslov,[16] T. Suzuki,[56] A. Taffard,[25,g] R. Takashima,[41] Y. Takeuchi,[56] R. Tanaka,[41] M. Tecchio,[35] P. K. Teng,[1] K. Terashi,[51] J. Thom,[18,i] A. S. Thompson,[22] G. A. Thompson,[25] E. Thomson,[46] P. Tipton,[61] P. Ttito-Guzmán,[32] S. Tkaczyk,[18] D. Toback,[54] S. Tokar,[15] K. Tollefson,[36] T. Tomura,[56] D. Tonelli,[18] S. Torre,[20] D. Torretta,[18] P. Totaro,[55a,55b] S. Tourneur,[45] M. Trovato,[47a] S.-Y. Tsai,[1] Y. Tu,[46] N. Turini,[47a,47c] F. Ukegawa,[56] S. Vallecorsa,[21] N. van Remortel,[24,c] A. Varganov,[35] E. Vataga,[47a,47d] F. Vázquez,[19,m] G. Velev,[18] C. Vellidis,[3] M. Vidal,[32] R. Vidal,[18] I. Vila,[12] R. Vilar,[12] T. Vine,[31] M. Vogel,[38] I. Volobouev,[29,s] G. Volpi,[47a,47b] P. Wagner,[46] R. G. Wagner,[2] R. L. Wagner,[18] W. Wagner,[27,v] J. Wagner-Kuhr,[27] T. Wakisaka,[42] R. Wallny,[9] S. M. Wang,[1] A. Warburton,[34] D. Waters,[31] M. Weinberger,[54] J. Weinelt,[27] W. C. Wester III,[18] B. Whitehouse,[57] D. Whiteson,[46,g] A. B. Wicklund,[2] E. Wicklund,[18] S. Wilbur,[14] G. Williams,[34] H. H. Williams,[46] P. Wilson,[18] B. L. Winer,[40] P. Wittich,[18,i] S. Wolbers,[18] C. Wolfe,[14] T. Wright,[35] X. Wu,[21] F. Würthwein,[10] S. Xie,[33] A. Yagil,[10] K. Yamamoto,[42] J. Yamaoka,[17] U. K. Yang,[14,o] Y. C. Yang,[28] W. M. Yao,[29] G. P. Yeh,[18] J. Yoh,[18] K. Yorita,[58] T. Yoshida,[42] G. B. Yu,[50] I. Yu,[28] S. S. Yu,[18] J. C. Yun,[18] L. Zanello,[52a,52b] A. Zanetti,[55a] X. Zhang,[25] Y. Zheng,[9,e] and S. Zucchelli[6a,6b]

(CDF Collaboration)

[1]*Institute of Physics, Academia Sinica, Taipei, Taiwan 11529, Republic of China*
[2]*Argonne National Laboratory, Argonne, Illinois 60439*
[3]*University of Athens, 157 71 Athens, Greece*
[4]*Institut de Fisica d'Altes Energies, Universitat Autonoma de Barcelona, E-08193, Bellaterra (Barcelona), Spain*
[5]*Baylor University, Waco, Texas 76798*
[6a]*Istituto Nazionale di Fisica Nucleare Bologna, I-40127 Bologna, Italy*
[6b]*University of Bologna, I-40127 Bologna, Italy*
[7]*Brandeis University, Waltham, Massachusetts 02254*
[8]*University of California, Davis, Davis, California 95616*
[9]*University of California, Los Angeles, Los Angeles, California 90024*
[10]*University of California, San Diego, La Jolla, California 92093*
[11]*University of California, Santa Barbara, Santa Barbara, California 93106*
[12]*Instituto de Fisica de Cantabria, CSIC-University of Cantabria, 39005 Santander, Spain*
[13]*Carnegie Mellon University, Pittsburgh, Pennsylvania 15213*
[14]*Enrico Fermi Institute, University of Chicago, Chicago, Illinois 60637*
[15]*Comenius University, 842 48 Bratislava, Slovakia; Institute of Experimental Physics, 040 01 Kosice, Slovakia*
[16]*Joint Institute for Nuclear Research, RU-141980 Dubna, Russia*
[17]*Duke University, Durham, North Carolina 27708*
[18]*Fermi National Accelerator Laboratory, Batavia, Illinois 60510*
[19]*University of Florida, Gainesville, Florida 32611*
[20]*Laboratori Nazionali di Frascati, Istituto Nazionale di Fisica Nucleare, I-00044 Frascati, Italy*
[21]*University of Geneva, CH-1211 Geneva 4, Switzerland*
[22]*Glasgow University, Glasgow G12 8QQ, United Kingdom*
[23]*Harvard University, Cambridge, Massachusetts 02138*

[24]Division of High Energy Physics, Department of Physics,
University of Helsinki and Helsinki Institute of Physics, FIN-00014, Helsinki, Finland
[25]University of Illinois, Urbana, Illinois 61801
[26]The Johns Hopkins University, Baltimore, Maryland 21218
[27]Institut für Experimentelle Kernphysik, Universität Karlsruhe, 76128 Karlsruhe, Germany
[28]Center for High Energy Physics: Kyungpook National University, Daegu 702-701, Korea;
Seoul National University, Seoul 151-742, Korea; Sungkyunkwan University, Suwon 440-746, Korea;
Korea Institute of Science and Technology Information, Daejeon, 305-806, Korea;
Chonnam National University, Gwangju, 500-757, Korea
[29]Ernest Orlando Lawrence Berkeley National Laboratory, Berkeley, California 94720
[30]University of Liverpool, Liverpool L69 7ZE, United Kingdom
[31]University College London, London WC1E 6BT, United Kingdom
[32]Centro de Investigaciones Energeticas Medioambientales y Tecnologicas, E-28040 Madrid, Spain
[33]Massachusetts Institute of Technology, Cambridge, Massachusetts 02139
[34]Institute of Particle Physics: McGill University, Montréal, Québec, Canada H3A 2T8;
Simon Fraser University, Burnaby, British Columbia, Canada V5A 1S6;
University of Toronto, Toronto, Ontario, Canada M5S 1A7;
and TRIUMF, Vancouver, British Columbia, Canada V6T 2A3
[35]University of Michigan, Ann Arbor, Michigan 48109
[36]Michigan State University, East Lansing, Michigan 48824
[37]Institution for Theoretical and Experimental Physics, ITEP, Moscow 117259, Russia
[38]University of New Mexico, Albuquerque, New Mexico 87131
[39]Northwestern University, Evanston, Illinois 60208
[40]The Ohio State University, Columbus, Ohio 43210
[41]Okayama University, Okayama 700-8530, Japan
[42]Osaka City University, Osaka 588, Japan
[43]University of Oxford, Oxford OX1 3RH, United Kingdom
[44a]Istituto Nazionale di Fisica Nucleare, Sezione di Padova-Trento, I-35131 Padova, Italy
[44b]University of Padova, I-35131 Padova, Italy
[45]LPNHE, Universite Pierre et Marie Curie/IN2P3-CNRS, UMR7585, Paris, F-75252 France
[46]University of Pennsylvania, Philadelphia, Pennsylvania 19104
[47a]Istituto Nazionale di Fisica Nucleare Pisa, I-56127 Pisa, Italy
[47b]University of Pisa, I-56127 Pisa, Italy
[47c]University of Siena, I-56127 Pisa, Italy
[47d]Scuola Normale Superiore, I-56127 Pisa, Italy
[48]University of Pittsburgh, Pittsburgh, Pennsylvania 15260
[49]Purdue University, West Lafayette, Indiana 47907
[50]University of Rochester, Rochester, New York 14627
[51]The Rockefeller University, New York, New York 10021

[a]Deceased.
[b]With visitors from University of Massachusetts Amherst, Amherst, Massachusetts 01003.
[c]With visitors from Universiteit Antwerpen, B-2610 Antwerp, Belgium.
[d]With visitors from University of Bristol, Bristol BS8 1TL, United Kingdom.
[e]With visitors from Chinese Academy of Sciences, Beijing 100864, China.
[f]With visitors from Istituto Nazionale di Fisica Nucleare, Sezione di Cagliari, 09042 Monserrato (Cagliari), Italy.
[g]With visitors from University of California Irvine, Irvine, CA 92697.
[h]With visitors from University of California Santa Cruz, Santa Cruz, CA 95064.
[i]With visitors from Cornell University, Ithaca, NY 14853.
[j]With visitors from University of Cyprus, Nicosia CY-1678, Cyprus.
[k]With visitors from University College Dublin, Dublin 4, Ireland
[l]With visitors from University of Edinburgh, Edinburgh EH9 3JZ, United Kingdom.
[m]With visitors from Universidad Iberoamericana, Mexico D.F., Mexico.
[n]With visitors from Queen Mary, University of London, London, E1 4NS, United Kingdom.
[o]With visitors from University of Manchester, Manchester M13 9PL, United Kingdom.
[p]With visitors from Nagasaki Institute of Applied Science, Nagasaki, Japan.
[q]With visitors from University of Notre Dame, Notre Dame, IN 46556.
[r]With visitors from University de Oviedo, E-33007 Oviedo, Spain.
[s]With visitors from Texas Tech University, Lubbock, TX 79409.
[t]With visitors from IFIC(CSIC-Universitat de Valencia), 46071 Valencia, Spain.
[u]With visitors from University of Virginia, Charlottesville, VA 22904.
[v]With visitors from Bergische Universität Wuppertal, 42097 Wuppertal, Germany.
[w]On leave from J. Stefan Institute, Ljubljana, Slovenia.

[52a]*Istituto Nazionale di Fisica Nucleare, Sezione di Roma 1, Italy*
[52b]*Sapienza Università di Roma, I-00185 Roma, Italy*
[53]*Rutgers University, Piscataway, New Jersey 08855*
[54]*Texas A&M University, College Station, Texas 77843*
[55a]*Istituto Nazionale di Fisica Nucleare Trieste/Udine, I-34100 Trieste, Italy*
[55b]*University of Trieste/Udine, I-33100 Udine, Italy*
[56]*University of Tsukuba, Tsukuba, Ibaraki 305, Japan*
[57]*Tufts University, Medford, Massachusetts 02155*
[58]*Waseda University, Tokyo 169, Japan*
[59]*Wayne State University, Detroit, Michigan 48201*
[60]*University of Wisconsin, Madison, Wisconsin 53706*
[61]*Yale University, New Haven, Connecticut 06520*
(Received 24 December 2008; published 10 April 2009)

We report a measurement of the top quark mass, m_t, obtained from $p\bar{p}$ collisions at $\sqrt{s} = 1.96$ TeV at the Fermilab Tevatron using the CDF II detector. We analyze a sample corresponding to an integrated luminosity of 1.9 fb^{-1}. We select events with an electron or muon, large missing transverse energy, and exactly four high-energy jets in the central region of the detector, at least one of which is tagged as coming from a b quark. We calculate a signal likelihood using a matrix element integration method, where the matrix element is modified by using effective propagators to take into account assumptions on event kinematics. Our event likelihood is a function of m_t and a parameter JES (jet energy scale) that determines *in situ* the calibration of the jet energies. We use a neural network discriminant to distinguish signal from background events. We also apply a cut on the peak value of each event likelihood curve to reduce the contribution of background and badly reconstructed events. Using the 318 events that pass all selection criteria, we find $m_t = 172.7 \pm 1.8(\text{stat} + \text{JES}) \pm 1.2(\text{syst})$ GeV$/c^2$.

DOI: 10.1103/PhysRevD.79.072001 PACS numbers: 14.65.Ha

I. INTRODUCTION

The top quark mass, m_t, is an important parameter in the standard model of particle physics. Since the discovery of the top quark in 1995, there have been many reported measurements of its mass, all from the CDF and D0 experiments at the Fermilab Tevatron [1]. The standard model relates the top quark and W boson masses to the mass of the predicted Higgs boson via loop corrections. Precision measurements of m_t and the W boson mass m_W, in conjunction with many other precision electroweak measurements, thus provide constraints on the value of the Higgs boson mass [2].

The measurement reported here uses $p\bar{p}$ collision data corresponding to an integrated luminosity of 1.9 fb^{-1}, collected by the CDF II detector during Run II of the Fermilab Tevatron collider at $\sqrt{s} = 1.96$ TeV. In $p\bar{p}$ collisions, top quarks are produced predominantly as $t\bar{t}$ pairs, and present measurements within the standard model framework indicate that the top quark decays to a W boson and a b quark nearly 100% of the time [3]. The W boson can decay into either a charged lepton and a neutrino (''leptonic decay'') or a quark-antiquark pair (''hadronic decay''). We select events in which one of the W bosons decays leptonically and the other decays hadronically, where the lepton in the leptonic decay is required to be an electron or muon; this channel is referred to as the ''lepton + jets'' channel. Decays of W bosons into a tau lepton are not explicitly included in our model, although some events containing a tau lepton which decays into an electron or muon do pass our selection criteria and amount to approximately 7% of the $t\bar{t}$ signal. In general, an event in our candidate sample has four high-energy jets (two of which come from the parton shower and hadronization associated with the quarks from the hadronic W boson decay and two from the parton shower and hadronization of the b quarks), a charged electron or muon, and an unobserved neutrino. For a given Tevatron integrated luminosity, the lepton + jets channel allows for more precise measurements than channels in which both W bosons decay leptonically or hadronically, as it offers the best balance of available statistics and sample purity. The most recent m_t measurements obtained at the Tevatron using the lepton + jets topology are reported in Ref. [4].

The method we use to extract the top quark mass from a sample of candidate $t\bar{t}$ events is a modified matrix element integration method. The matrix element approach to the top quark mass measurement [5] is based on integrating over the tree-level phase space of the process, where each kinematic configuration of the tree-level partons is weighted by the matrix element squared and by the probability that the detector observables can be produced by the final-state particles. With an appropriate normalization factor, this integral defines the probability to see an event with this configuration in the detector. By multiplying the individual event probabilities, we obtain a likelihood, as a function of m_t, of seeing the event sample observed in our detector.

In theory, the distributions of the invariant masses of the top quark and the W boson decay products are dominated

by propagator-induced terms in the matrix element squared. The top quark and the W boson widths are relatively narrow in comparison with their respective masses. This leads to nearly pure relativistic Breit-Wigner distributions for the invariant masses of their decay products. Compared to this theoretical prediction, finite resolution of the detector measurement naturally results in a widening of the observed distributions. We describe the widening due to an imperfect measurement of magnitudes of jet momenta in terms of detector transfer functions. Effects of other uncertainties, such as finite angular resolutions, are modeled by replacing the Breit-Wigner terms in the matrix element squared with empirically determined distributions called ''effective propagators'' in this paper. This modification of the matrix element improves the observation model for $t\bar{t}$ events.

The matrix element used in this work [6] includes $t\bar{t}$ production, from both quark-antiquark and gluon-gluon collisions, and decay into the lepton + jets channel. Since we do not know which jet observed in our detector corresponds to which parton in the matrix element, we calculate the likelihood for each possible assignment of jets to partons and sum the likelihood over all permutations. Each permutation includes a weight, which takes into account the probability that the permutation is consistent with the observed information on whether the jet has been tagged or not as a b-jet. Tagging of b-jets is done by the displaced vertex technique discussed in Sec. III. For each permutation, the matrix element integration is performed over the seven kinematic variables in the event that remain after a set of simplifying assumptions.

We improve the precision of the method by introducing another parameter into our likelihood, the jet energy scale (JES). This is a scale factor which multiplies the energy of all jets. The uncertainty on the jet energy scale is the major source of systematic uncertainty on the top mass measurement; by including JES as a parameter in the likelihood, we can use the W boson decay to hadrons in the $t\bar{t}$ decay chain to provide *in situ* calibration, thus reducing the systematic uncertainty due to JES. Our final likelihood calculated for each candidate event is thus a function of both the top quark mass and JES.

Our model is designed to fit lepton + jets $t\bar{t}$ events where the final objects observed in the event come directly from $t\bar{t}$ decays. We thus need to take into account non-$t\bar{t}$ events or $t\bar{t}$ events where some of the observed objects do not originate from $t\bar{t}$ decay. The probability that a $t\bar{t}$ candidate event is background is estimated using a neural network output that is a function of several shape and kinematic variables, and then their expected contribution to the likelihood is subtracted from the total likelihood. In addition, we cut on the magnitude of the peak of the likelihood for an event to further reduce background and badly modeled events.

We multiply the individual likelihood curves from each event to get an overall likelihood. Because of the assumptions made, and the presence of background events, the extraction of a mass value and its uncertainty needs a calibration, which we obtain from Monte Carlo simulated events.

Section II is a brief description of the CDF II detector and its use for the measurements needed in this analysis. Section III defines the data sample used for this analysis and the estimated background. Section IV describes the likelihood construction for $t\bar{t}$ signal events. Section V explains how non-$t\bar{t}$ events are incorporated into the likelihood function. Section VI describes how the method is tested and calibrated. Section VII covers the systematic uncertainties. Section VIII summarizes the results obtained by applying the method to the data. Finally, Section IX gives the conclusions.

II. THE CDF II DETECTOR

A complete description of the CDF II detector and its use in lepton, jet, and secondary vertex reconstruction can be found elsewhere [7]. Here, we describe the components that are essential for this analysis and how they are used.

The CDF II detector is a general-purpose detector with a cylindrical geometry featuring forward-backward symmetry and axial symmetry around the beam pipe. The CDF coordinate system uses a cylindrical system centered at the interaction point with the z (longitudinal) axis along the proton beam direction, r the distance to the beam line, and ϕ the azimuthal angle around the beam line. We also use θ, the polar angle from the beam line. The pseudorapidity η of a particle three-momentum is defined in terms of the polar angle θ by $\eta = -\ln(\tan(\theta/2))$. For a particle with momentum p and energy E, we define the transverse momentum p_T and the transverse energy E_T as $p\sin\theta$ and $E\sin\theta$, respectively. The detector covers the complete solid angle in θ and ϕ up to $|\eta| = 3.6$.

The innermost part of the detector consists of the charged particle tracking detectors, which are immersed in a 1.4 T magnetic field provided by a superconducting solenoid oriented parallel to the beam line. Calorimeters and muon systems outside the solenoid provide lepton measurement and identification in addition to jet momentum measurements. The tracking detectors and calorimeters together provide identification of jets from heavy (charm and bottom) quarks.

The first component of the tracking system is a series of silicon microstrip detectors between radii of 1.5 and 28 cm. The innermost layer (L00) [8] is a single-sided layer of silicon attached directly to the beam pipe, providing a position measurement very close to the collision point. Five layers of double-sided microstrip detectors (SVXII) cover up to $r = 10.6$ cm in the $|\eta| < 1.0$ region [9]. Each layer has one side with strips oriented parallel to the beam line to provide measurements in the r-ϕ plane and one side at a stereo angle to provide three-dimensional measurements; two layers have strips at a 90° angle and three

layers have strips at a 1.2° angle. The ISL [10] is an additional set of silicon microstrip detectors located outside of SVXII to provide measurements at larger distances from the beam line, thus improving the silicon tracking. It consists of one layer at $r = 22$ cm in the central region ($|\eta| < 1.0$) and two layers at $r = 20$ cm and $r = 28$ cm in the forward region ($1.0 < |\eta| < 2.0$). The typical resolution of these detectors in the r-ϕ plane is 11 μm. The impact parameter resolution of this system is $\sigma(d_0) \approx 40$ μm, of which approximately 35 μm is due to the transverse size of the Tevatron interaction region. Outside of the silicon layers lies the central outer tracker (COT) [11], an open-cell drift chamber detector, which provides coverage for $|\eta| < 1.0$. Multiple wire planes, each with 12 sense wires, are grouped in 8 superlayers which extend to a radius of 137 cm. The superlayers alternate between having wires parallel to the beam axis and wires skewed by a ±2° stereo angle, thus providing up to 96 points for track reconstruction. Together with the additional constraint coming from the primary vertex position, these tracking elements provide a resolution on the track transverse momentum, p_T, of $\sigma(p_T)/p_T \approx 0.1\% \cdot p_T/(\mathrm{GeV}/c)$.

Outside the tracking system and the solenoid are segmented electromagnetic and hadronic calorimeters. The central calorimeter covers up to $|\eta| < 1.1$ and has a projective geometry consisting of towers segmented in η and ϕ pointing toward the center of the detector. The central electromagnetic calorimeter (CEM) consists of alternating layers of lead plates and plastic scintillators, 18 radiation lengths deep. The energy detected in small contiguous groups of calorimeter towers is summed into electromagnetic clusters. These clusters are identified as electron candidates if they match a track reconstructed in the tracking system and if very little energy is detected in the surrounding towers (i.e., if the cluster is isolated). The energy resolution for an electron with tranverse energy E_T is given by $\sigma(E_T)/E_T \approx 13.5\%/\sqrt{E_T/\mathrm{GeV}} \oplus 2\%$. Approximately at shower maximum are proportional strip and wire chambers (CES) which provide finer position resolution for electron and photon identification. The central hadronic calorimeter (CHA) is composed of alternating layers of iron plates and scintillators, 4.5 nuclear interaction lengths deep, again with projective geometry segmentation. A plug tile calorimeter covers the forward region with $1.1 < |\eta| < 3.6$, consisting of a lead/scintillator electromagnetic portion (PEM), scintillator strips at shower maximum (PES), and an iron/scintillator hadronic portion (PHA). An additional hadronic calorimeter (WHA) covers the region between the plug calorimeter and the central calorimeter and improves the hermeticity of the detector. These calorimeters provide jet measurements with a resolution of approximately $\sigma(E_T) \approx 0.1 \cdot E_T + 1.0$ GeV [12].

In the central and forward regions, jets are reconstructed with a cone algorithm [12], which adds groups of electromagnetic (E_{EM}) and hadronic clusters (E_{HAD}) that fall within a cone of radius $\Delta R = \sqrt{\Delta\phi^2 + \Delta\eta^2} \leq 0.4$ around a seed tower with energy of at least 1 GeV. The jet energies are corrected for multiple primary interactions (pileup) and for detector effects including a calibrated nonlinearity in the calorimeter and average losses in nonsensitive regions of the calorimeter. The jet energies are also corrected for hadronic physics effects. Soft hadroproduction in the underlying event tends to increase the measured jet energy, while the limited cone size of the jet clustering algorithm gives rise to out-of-cone losses [13]. Uncertainties for each of these corrections contribute to the jet systematic uncertainty, and are used to assign an uncertainty on the top quark mass.

In the lepton + jets channel one of the W bosons decays into a lepton and a neutrino, which escapes undetected. This results in less energy being measured in our detector than we would otherwise expect. We require this as a signature for $t\bar{t}$ events. Specifically, we define a quantity, the missing E_T ($\not\!\!E_T$), to measure the resulting transverse energy imbalance as follows:

$$\not\!\!E_T = \left| \sum_{i \in \mathrm{towers}} E_{T_i} \hat{n}_{T_i} \right|, \tag{1}$$

where $\hat{n}_{T_i}$ is the unit vector in the x-y plane pointing from the primary vertex to a given calorimeter tower and E_{T_i} is the uncorrected E_T measured in that tower. Two corrections to this quantity are made. One is to account for muons, which, unlike other particles, typically deposit only a small fraction of their energy in the towers, and the other is to take into account the corrections applied to the raw energies of the jets. Details of these corrections can be found in Ref. [14].

Muon identification takes place in three separate subdetectors. Two of these are in the central region: one set of four layers of drift chambers (CMU) located outside the central calorimeters (after 4.6 hadronic absorption lengths of material), and another set of four layers (CMP) located outside the magnet return yoke, which provides an additional 60 cm of absorbing steel. Muon tracks in this region are required to pass through both detectors and are called CMUP muons. These two subdetectors cover the region $|\eta| \leq 0.6$. Muons in the region $0.6 < |\eta| < 1.0$ are detected by an additional set of four layers of drift chambers (CMX), completing the full fiducial region of the COT. CMUP or CMX track segments are matched to tracks in the COT; in addition, the energy deposited in the CEM and CHA is required to be small.

The trigger system is used to record events with high-p_T leptons. The trigger is a three-level filter in which the first two levels use specialized hardware and utilize only the detector subsystems with fast readout. The third level is a complete reconstruction of the event using the same software used for the offline reconstruction, but with less stringent cuts. The level 1 (L1) trigger uses information

from the calorimeter clusters and from the XFT (eXtremely Fast Tracker), which reconstructs tracks from the COT r-ϕ information with a momentum resolution given by $\sigma(p_T)/p_T \approx 2\% \cdot p_T/(\mathrm{GeV}/c)$ [15]. The L1 central electron trigger requires a track with $p_T > 8$ GeV/c pointing to a tower with $E_T > 8$ GeV and $E_{\mathrm{HAD}}/E_{\mathrm{EM}} < 0.125$. The L2 trigger adds clustering in the CEM calorimeter and requires that a cluster with $E_T > 16$ GeV matches with a $p_T > 8$ GeV/c track. The L1 and L2 muon triggers require a track with $p_T > 4$ GeV/c (CMUP) or $p_T > 8$ GeV/c (CMX) pointing to a track segment in the respective drift chamber system. A complete lepton reconstruction is performed in the L3 trigger, where $E_T > 18$ GeV is required for electrons and $p_T > 18$ GeV/c is required for muons.

III. DATA SAMPLE AND BACKGROUND

As mentioned previously, we search for events in the lepton + jets topology, where a $t\bar{t}$ pair is produced, each top quark decays into a W boson and a b quark, and one W boson decays leptonically and one hadronically. We thus identify our top quark candidates by selecting events with four high-energy jets, a high-energy electron or muon, and $\not\!\!E_T$ from a neutrino. Specifically, we require either an electron with $E_T > 20$ GeV or a muon with $p_T > 20$ GeV/c in the central region ($|\eta| < 1.0$) of the detector. Electron and muon identification criteria are discussed in Ref. [7]. For the neutrino, we require $\not\!\!E_T > 20$ GeV in the event. We require exactly four jets with $E_T > 20$ GeV and pseudorapidity $|\eta| < 2.0$. The jet E_T is corrected for pileup, inhomogeneities of the detector, and nonlinear calorimeter response as a function of jet p_T and η [13]. The additional corrections (underlying event and out-of-cone losses) are not used in the analysis, but their uncertainties are taken into account in evaluating the systematic uncertainties on the final result.

Non-$t\bar{t}$ events that contain a W boson and four jets are able to pass the aforementioned selection cuts. However, most of these events do not contain b quarks in their final state, while $t\bar{t}$ events will nearly always have two b quarks. The b quarks from top quark decay hadronize into B-hadrons with energies on the order of several tens of GeV, due to the high mass of the parent top quark. Since the B-hadron decay time is approximately 1.5 ps, it is possible to reconstruct secondary vertices within a jet using the charged particles from the B decay [16]. A jet with an identified secondary vertex is called a b-tagged jet. Therefore, to further increase the $t\bar{t}$ purity of the sample, we require that at least one of the jets must be tagged as a b-jet using a secondary vertex tagging algorithm.

The outline of the b-tagging algorithm used, SECVTX, is as follows: first, the charged particle tracks in the jet are subjected to selection cuts to ensure that a quality secondary vertex can be reconstructed. There must either be at least three tracks with $p_T \geq 0.5$ GeV/c where at least one of the tracks must be ≥ 1 GeV/c, or at least two tracks with $p_T \geq 1$ GeV/c. Once the secondary vertex is reconstructed using the tracks, the distance in the x-y plane between the primary and secondary vertices is projected onto the direction of the jet; this quantity is referred to as $L_{2\mathrm{D}}$ (see Fig. 1). A jet is tagged if $L_{2\mathrm{D}} > 7.5\sigma_{L_{2\mathrm{D}}}$, where $\sigma_{L_{2\mathrm{D}}}$, the uncertainty on $L_{2\mathrm{D}}$, is approximately 190 μm. For b-jets produced in $t\bar{t}$ decay, the b-tagging efficiency is about 40%, while light jets are misidentified as b-jets with a rate of less than 2%. For more details see Ref. [16].

In 1.9 fb^{-1} of data we find 371 $t\bar{t}$ candidate events that pass the above selection requirements, 284 of which have one b-tag and 87 of which have more than one b-tag (see Table I); 207 of the candidate events contain an electron and 164 contain a muon. The background to the $t\bar{t}$ signal consists of three main sources: a) events where a W boson is produced in conjunction with heavy flavor quarks ($b\bar{b}$, $c\bar{c}$, or c); b) events where a W boson is produced along with light flavor quarks where a light flavor jet has been incorrectly tagged with a b-tag (mistag); c) QCD events, which do not contain a W boson (non-W events) but have a jet mimicking a lepton, a jet with a b-tag, and $\not\!\!E_T$. There are also smaller contributions from single top quark production, diboson (WW, WZ, or ZZ) production, and Z + jets production. The estimated number of background events for each of these sources is derived with the method used for the cross section measurement [17].

The contributions for the various types of background shown in Table I are estimated as follows. First, we define a pretag event sample, which comprises all events that pass all the signal selection requirements except for the b-tag requirement; our final tagged samples are thus subsets of the pretag sample. For all samples, the expected number of events for diboson, Z + jets, and single top quark backgrounds, as well as the $t\bar{t}$ signal, are estimated using

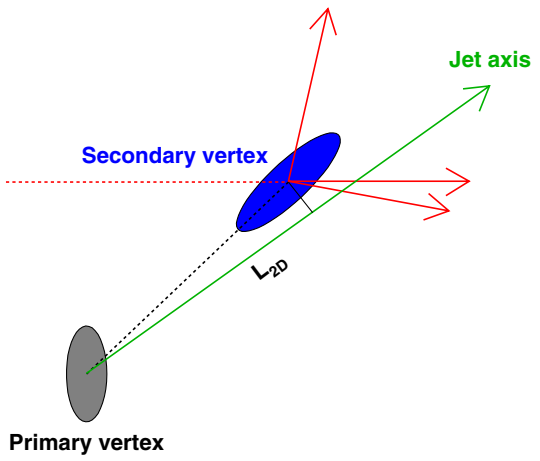

FIG. 1 (color online). A view of a b-jet in the x-y plane. $L_{2\mathrm{D}}$, the distance between the primary and secondary vertices projected onto the jet axis, along with its uncertainty, is used to determine whether a jet originates from a heavy flavor quark.

TABLE I. Summary of observed data and predicted $t\bar{t}$ signal and background contributions as a function of b-tags in the event.

Background	1 tag	≥ 2 tags
Non-W QCD	13.8 ± 11.5	0.5 ± 1.5
W + light flavor (mistag)	16.3 ± 3.6	0.3 ± 0.1
Diboson (WW, WZ, ZZ), Z + jets	5.5 ± 0.4	0.5 ± 0.1
$W + b\bar{b}$, $c\bar{c}$, c	26.1 ± 10.2	3.4 ± 1.4
Single top	3.0 ± 0.2	0.9 ± 0.1
Total background	64.7 ± 16.3	5.5 ± 2.6
Predicted $t\bar{t}$ signal	182.6 ± 24.6	69.4 ± 11.2
Events observed	284	87

Monte Carlo (MC) simulated events assuming the theoretical cross sections. To simulate the signal, we generate $t\bar{t}$ events at a variety of top quark masses from 152 GeV$/c^2$ to 190 GeV$/c^2$ (needed for our top mass analysis) using the PYTHIA MC generator version 6.216 [18]. As a cross-check we also use $t\bar{t}$ signal events generated with the HERWIG generator version 6.510 [19]. For the number of expected $t\bar{t}$ events used in the background estimate we use a top mass of 175 GeV$/c^2$, with a calculated $t\bar{t}$ production cross section of 6.7 ± 0.8 pb [20].

The non-W contribution is estimated by a fit to the observed $\not\!\!E_T$ distribution of expected $\not\!\!E_T$ distributions for non-W events (which lie mostly in the low $\not\!\!E_T$ region) and W + jets events. These distributions are taken from data sidebands (either events with leptons which fail to meet the isolation requirements, or from ''antielectron'' samples, which are electron candidates failing two other selection requirements) and from simulated MC events. This fit is performed separately for the pretagged and tagged samples to obtain the expected number of events in each.

The W + jets background contribution to the pretag sample is taken as the remainder after subtracting all the above pretag contributions. The relative contribution of W + heavy flavor events to the pretag W + jets contribution is estimated with MC simulation. We use MC events generated with the ALPGEN [21] generator (version 2.10 prime) along with PYTHIA version 6.325 to perform the parton shower and hadronization. The ALPGEN program is used to generate samples with specific numbers of partons in the matrix element; this decreases the time to generate

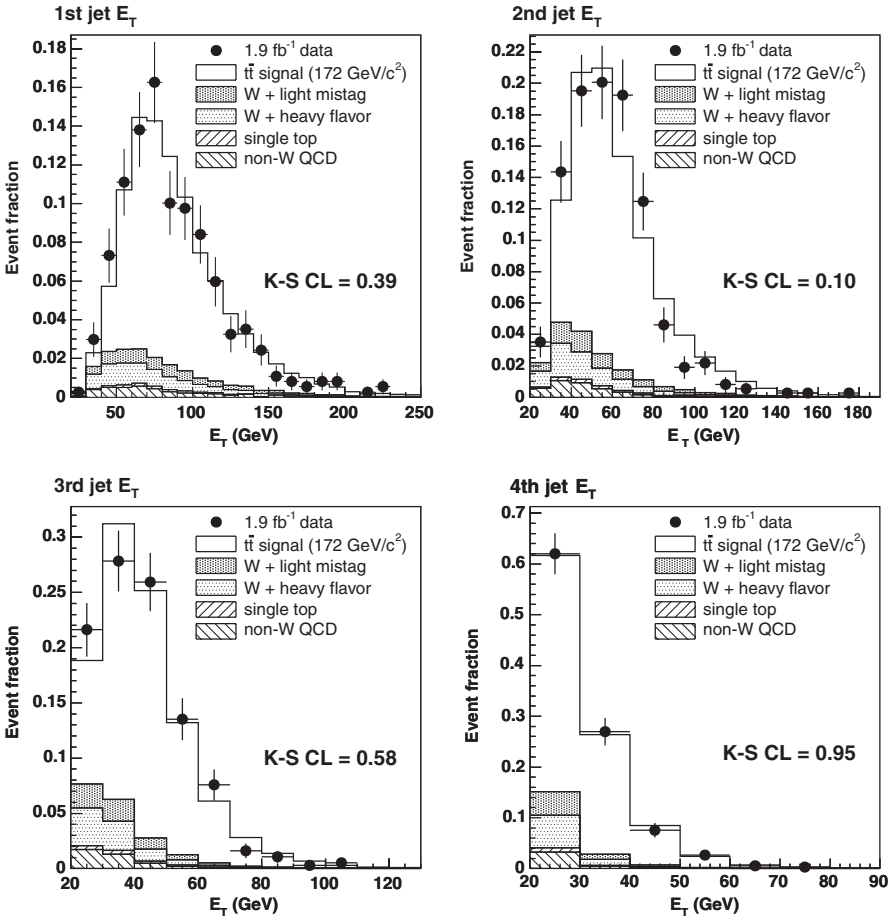

FIG. 2. Comparison of data and MC predictions for the selected events. The confidence level obtained from a K-S test on the two distributions is indicated on the histogram. The plots show, in order, the corrected E_T of the leading jet, 2nd jet, 3rd jet, and 4th jet in our events.

events with high jet multiplicity. Since each sample contains a different number of partons (for instance, the $W + b\bar{b}$ sample contains $W + b\bar{b} + 0p$, $W + b\bar{b} + 1p$, and $W + b\bar{b} + \geq 2p$ contributions), we combine the separate samples using their expected fractions, and remove overlaps using the ALPGEN jet-parton matching along with a jet-based heavy flavor overlap removal algorithm [17]. Finally, applying heavy flavor and light flavor b-tag efficiencies we obtain the estimated $W +$ jets contributions to the final sample.

The single top quark contribution is generated using the MadGraph/MadEvent [22] package along with PYTHIA for the parton shower and hadronization. Since their expected contribution is small, we do not use separate MC samples for diboson or $Z +$ jets backgrounds, but rather merge them into the $W +$ light flavor total. All MC samples are simulated using the CDF II detector response simulation package [23].

Table I summarizes the data sample composition as a function of the number of tagged jets in the event. The total number of expected background events in our data sample is $N_{\mathrm{bg}} = 70.3 \pm 16.5$ out of 371 observed events.

We test our background model by comparing selected kinematic distributions in the data with those expected by our model, by adding the MC samples used for the $t\bar{t}$ signal and backgrounds and the data samples used for the QCD background according to their predicted proportions.

Figures 2 and 3 show the comparisons. All of these plots require exactly four jets with $E_T > 20$ GeV and $|\eta| < 2.0$, but in Fig. 3, we also show the number of jets with lower energies for an additional comparison between data and MC. For each quantity, we perform a Kolmogorov-Smirnov (K-S) test comparing the data and MC samples; in all cases, the resulting confidence level shows a good agreement, which validates the use of the MC generators and the QCD background used in this analysis.

IV. SIGNAL LIKELIHOOD

The matrix element method allows for efficient incorporation of the theoretical assumptions about the process under study into the data analysis. The phase space integration procedure can be viewed as a Bayesian marginalization of the event probability over all unobserved

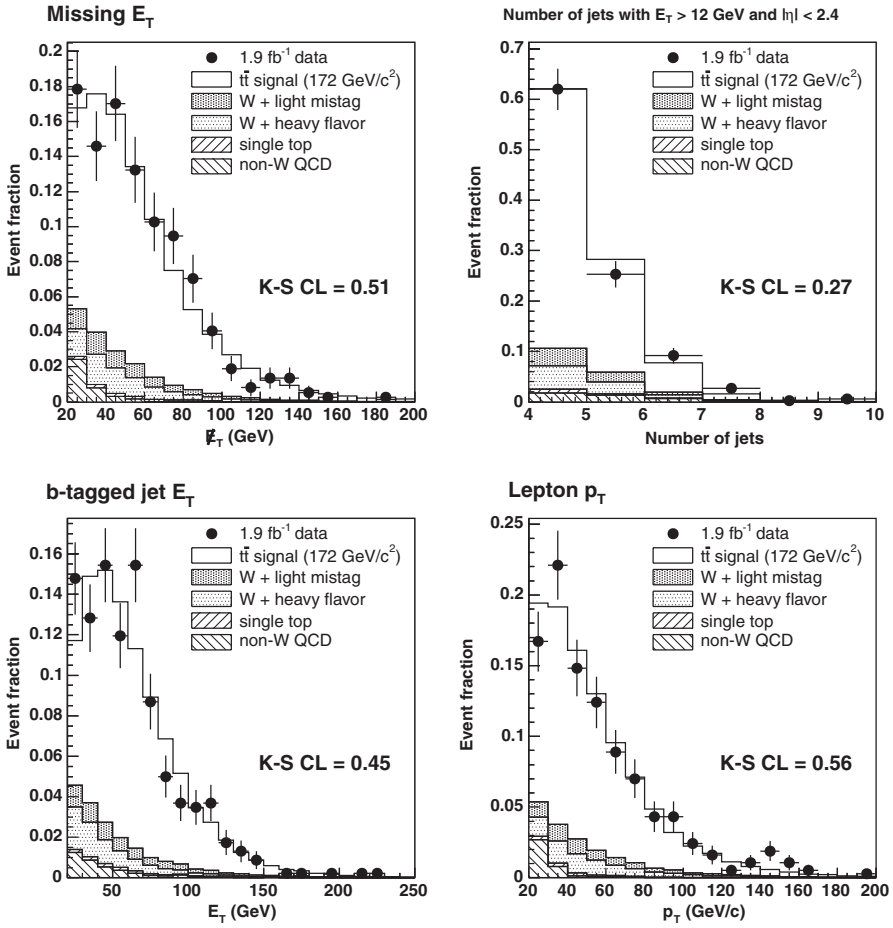

FIG. 3. Comparison of data and MC predictions for the selected events. The confidence level obtained from a K-S test on the two distributions is indicated on the histogram. The plots show, in order, the event $\not\!\!E_T$, the total number of jets with $E_T > 12$ GeV and $|\eta| < 2.4$ in the event, the E_T for all jets with a b-tag, and the lepton p_T.

degrees of freedom. Particle theory provides a well-motivated informative prior for this marginalization. Maximization of the likelihood with respect to the measured parameters results in an efficient (in the statistical sense) estimate of these parameters.

Instead of attempting to integrate over the complete phase space of the process which can include hundreds of particles, we assume that the final-state parton showering and hadronization processes, together with the detector response, can be modeled empirically by the transfer functions. This assumption allows for a drastic reduction in the phase space complexity. However, calculation of the remaining tree-level phase space integrals still remains a formidable problem when a large number of events and parameter values must be processed. Therefore, we employ additional assumptions, detailed later in this section, to reduce the dimensionality. To compensate for these assumptions, we introduce the concept of "effective propagators" that modify the tree-level matrix element of the interaction.

For each event we obtain a $t\bar{t}$ signal probability as a function of the top quark pole mass (m_t) and the jet energy scale (JES) using the following expression:

$$L(\vec{y}|m_t, \mathrm{JES}) = \frac{1}{N(m_t)} \frac{1}{A(m_t, \mathrm{JES})} \times \sum_{i=1}^{24} w_i \int \frac{f(z_1)f(z_2)}{FF} \mathrm{TF}(\vec{y} \cdot \mathrm{JES}|\vec{x}) \times |M_{\mathrm{eff}}(m_t, \vec{x})|^2 d\Phi(\vec{x}), \quad (2)$$

where $\vec{y}$ are the quantities we measure in the detector (the momenta of the charged lepton and all the jets); $\vec{x}$ are the parton-level quantities that define the kinematics of the event; $N(m_t)$ is an overall normalization factor; $A(m_t, \mathrm{JES})$ is the event acceptance as a function of m_t and JES; $f(z_1)$ and $f(z_2)$ are the parton distribution functions (PDFs) for incoming parton momentum fractions z_1 and z_2; FF is the relativistic invariant flux; $\mathrm{TF}(\vec{y} \cdot \mathrm{JES} \mid \vec{x})$ are the transfer functions that predict the measured jet momenta distributions given the quark kinematics; $d\Phi(\vec{x})$ indicates integration over the phase space of the two initial and six final-state partons and leptons in the $t\bar{t}$ production and decay (including necessary Jacobians); and $M_{\mathrm{eff}}(m_t, \vec{x})$ is the modified matrix element for $t\bar{t}$ production and decay. The PDFs, $f(z_1)$ and $f(z_2)$, are integrated over the appropriate combinations of incoming $q\bar{q}$ and gluons. We use the CTEQ5L PDFs [24] in our integration. The integral is calculated for each of the 24 possible permutations of jet-parton assignment and then summed with the appropriate weights w_i, where the weights are determined by the b-tagging information on the jets. Specifically, for each tagged jet in the event, a weight equal to the tag rate of the jet is given if it is assigned to a b parton, and a weight equal to the mistag rate is given if it is assigned to a light parton. An untagged jet is given a weight of 1 minus the tag rate if assigned to a b parton, and 1 minus the mistag rate if assigned to a light parton. The four individual jet weights are then multiplied. Figure 4 shows the parametrizations of the tag rates as a function of jet E_T and $|\eta|$ used to determine the w_i values; we assign a probability for a c

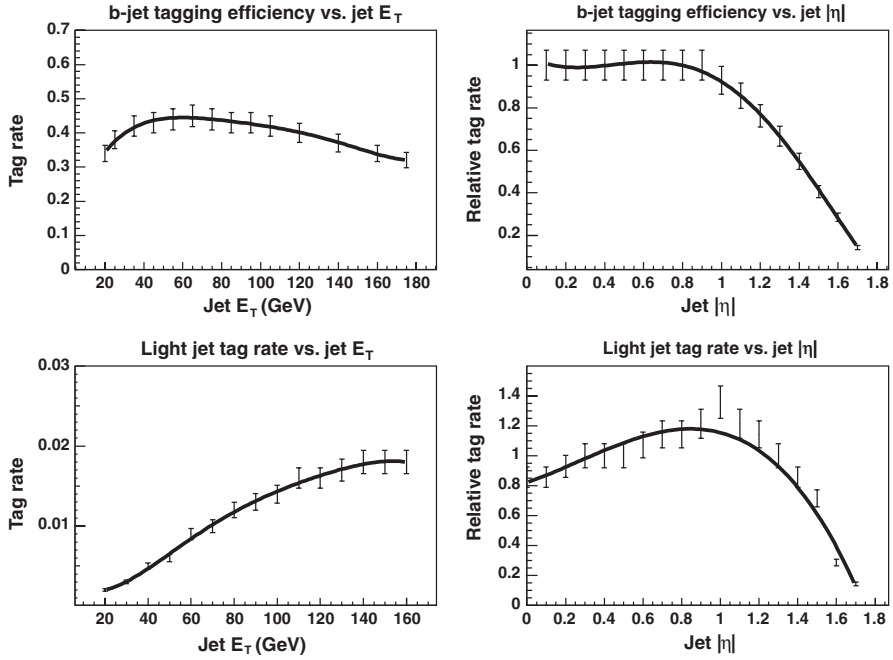

FIG. 4. Efficiency for the SECVTX algorithm with systematic uncertainties. The top two plots show the tag efficiency for tagging b-jets as a function of the jet E_T (left) and $|\eta|$ (right), and the bottom two plots show the tag rate for light jets (mistags), also as a function of jet E_T (left) and $|\eta|$ (right). The fits used as a parametrization in our analysis are also shown.

jet to be tagged equal to 0.22 times the probability for a b-jet with the same E_T and $|\eta|$. These values are derived from Monte Carlo events and then corrected with a scale factor measured in data to account for differing tag rates in Monte Carlo events and data events.

We begin with the Kleiss-Stirling matrix element [6], which includes both $q\bar{q} \rightarrow t\bar{t}$ and $gg \rightarrow t\bar{t}$ production processes, as well as all spin correlations. The integral formula in Eq. (2) requires a 24-dimensional integration (eight four-vectors are needed to describe the reaction, but energy-momentum conservation together with the negligible masses of the initial partons and the final-state leptons allow for a trivial phase space dimensionality reduction to 24). This is computationally difficult to evaluate, so we make the following simplifying assumptions: the lepton direction and momentum are perfectly measured; the directions of the partons coincide with the measured jet directions; the light-quark masses are zero, the b quark from the hadronic top quark is on mass shell, and the b quark from the leptonic top quark has zero mass. The last assumption results in a simplification of the kinematic equation on the leptonic side, from an 8th-order to a 4th-order polynomial. We introduce a prior for the transverse momentum of the $t\bar{t}$ system into the overall event probability formula, but we do not consider the transverse motion of individual initial partons. This allows us to eliminate two more integration variables. The $t\bar{t}$ transverse momentum prior, as constructed from HERWIG MC samples, is nearly independent of the top quark mass for masses between 120 and 220 GeV$/c^2$. The transverse momentum of the initial partons is also neglected for the determination of z_1 and z_2 from the event kinematics.

We choose the set of seven remaining variables of integration to be the squared masses M_t^2 and M_W^2 on both the leptonic decay and hadronic decay side of the $t\bar{t}$ system, $\beta = \log(p_q/p_{\bar{q}})$, where p_q and $p_{\bar{q}}$ are the magnitudes of the momenta of the two products from the hadronic W boson decay, and the two-dimensional transverse momentum vector $\vec{p}_T$ of the $t\bar{t}$ system. Note that the top quark and W boson pole masses, m_t and m_W, are not the same variables as M_t and M_W. The latter variables refer to the top quark and W boson masses in a given event, and we integrate over them in our likelihood calculation.

The expected distributions of M_t^2 and M_W^2 are defined almost exclusively by the top quark and W boson propagator terms in the matrix element. Nominally, these are relativistic Breit-Wigners peaked at the top quark and W boson masses; however, the kinematic assumptions to reduce the number of integration dimensions described above cause the M_t^2 and M_W^2 distributions to be altered from their Breit-Wigner form. To account for this, we replace the Breit-Wigner propagators in the matrix element with propagators that reflect the assumptions; we call these adjusted propagators "effective propagators."

A. Effective propagators

The effective propagators are built by calculating invariant masses of "effective partons." These objects are constructed in such a manner that their four-momenta can be reproduced exactly using only the integration variables and the variables measured in the detector by solving kinematic equations consistent with our assumptions. In each MC event, we find the assignment of the four tree-level partons to the four highest p_T jets reconstructed in the detector that minimizes the combined distance in the η-ϕ space between partons and jets. Then we construct effective partons by building four-vectors that have the energies of the tree-level partons, the directions of the matched calorimeter jets, and the masses used in the kinematic equation solvers (i.e., zero for light quarks and the leptonic side b, and 4.95 GeV$/c^2$ for the hadronic side b). We associate effective values of top quark and W boson mass, as well as β and $\vec{p}_T(t\bar{t})$, by building these quantities out of the effective partons. The effective partons are also used in the construction of our calorimeter transfer functions, for the sake of consistency.

The construction of the effective propagator on the leptonic side uses values of the lepton momentum smeared according to the Gaussian resolution functions given in Sec. II: $\sigma(p_T)/p_T = 0.1\% \cdot p_T/(\mathrm{GeV}/c)$ for muons and $\sigma(E_T)/E_T = 13.5\%/\sqrt{E_T/\mathrm{GeV}} \oplus 2\%$ for electrons.

The choice of the neutrino p_z is ambiguous; for each event we solve for the p_z that minimizes the deviation of the effective leptonic W boson and top quark masses, $M_{W,\mathrm{eff}}$ and $M_{t,\mathrm{eff}}$, from the tree-level W boson mass, $M_{W,\mathrm{gen}}$, and top quark mass, $M_{t,\mathrm{gen}}$. The deviation is quantified by a χ^2 defined as

$$\chi^2 = \frac{(M^2_{t,\mathrm{eff}} - M^2_{t,\mathrm{gen}})^2}{\sigma_t^2} + \frac{(M^2_{W,\mathrm{eff}} - M^2_{W,\mathrm{gen}})^2}{\sigma_W^2}, \quad (3)$$

where

$$\sigma_t = \Gamma_t m_t, \qquad \sigma_W = \Gamma_W m_W, \quad (4)$$

m_t and m_W are pole masses for the top quark and the W boson, and Γ_t and Γ_W are their decay widths. When this p_z search is performed, the transverse momentum of the leptonic-side top quark is set to the difference between the tree-level MC value of the $t\bar{t}$ transverse momentum and the effective transverse momentum of the hadronic-side top quark.

In our calculations we assume that there is no correlation between the effective propagators on the hadronic and leptonic sides of the event. In reality, the invariant masses on the leptonic side are affected by the hadronic side uncertainties due to the definition of the leptonic top quark momentum used in the effective propagator construction. However, the uncertainty due to the transverse momentum transfer from the hadronic to the leptonic side is not large

in comparison with the uncertainty associated with the unknown transverse momentum of the $t\bar{t}$ system itself.

The widening of the effective invariant masses in comparison with the original Breit-Wigner distributions depends on the event kinematics. For example, finite angular resolution of the detector results in the greatest widening of the effective W boson mass distribution on the hadronic side when the opening angle between the two jets originating from the W boson decay is close to $\pi/2$. Because of the large dimensionality of the phase space and limited CPU resources available, it is not feasible to model the shapes of the effective invariant mass distributions for each kinematic configuration encountered in the calculation of event probabilities. Instead, we characterize these shapes using a low-dimensional quantity with high predictive power: the covariance matrix for effective W boson and top quark masses.

On the hadronic side of the event we calculate the appropriate Jacobian and propagate the uncertainties from jet masses and angles to M_t^2 and M_W^2 using the standard, first-order multivariate error propagation formulae. We assume that the uncertainties of jet masses and angles are not correlated. The angular resolutions calculated with HERWIG and used to build the hadronic-side propagators are shown in Fig. 5, where the angular resolution is defined as the width of the $\Delta\eta$ or $\Delta\phi$ distribution in a given parton p_T bin. The resolution on the jet mass squared used for covariance matrix estimation is assumed to be constant: $\sigma(m^2) = 242\ \mathrm{GeV}^2/c^4$ for b-jets and $\sigma(m^2) = 202\ \mathrm{GeV}^2/c^4$ for light jets. (These values are also calculated with HERWIG.) The uncertainties on the magnitudes of the parton momenta are not used to build this covariance matrix—these uncertainties are taken into account by the transfer functions.

Three independent quantities can be extracted from the covariance matrix constructed in this manner: the standard deviations for M_t^2 and M_W^2 and the correlation coefficient. We assume that the hadronic side effective propagator depends only on these three quantities. However, we do not make any functional assumption about the propagator shape. Instead, we use MC events to build a nonparametric estimate of the propagator density. We split the 3-D space of the two standard deviations and the correlation coefficient into cells that contain approximately equal numbers of events. In each cell, we use a kernel density estimation technique [25] to construct the effective propagator. The propagator is initially evaluated on a sufficiently dense rectangular grid, and fast linear interpolation is used to find its values during subsequent calculations. When the event is reconstructed during the likelihood integration, the covariance matrix is calculated for the given kinematics, and the corresponding effective propagator density is looked up in a table of precomputed propagators.

Because of the presence of the unobserved neutrino, the kinematic configuration on the leptonic side of the event is significantly less constrained than that on the hadronic side, and provides less information about the top quark mass and the jet energy scale. Because of this, we employ a simplified model for the leptonic side effective propagators. These propagators are averaged over various kinematic configurations, and they depend only on the assumed top quark pole mass, not on the kinematics of a particular event. (The hadronic side propagators depend on the top quark pole mass implicitly, via the Jacobians used in the error propagation.) Examples of the hadronic and leptonic side effective propagators are shown in Fig. 6. Note that ΔM_t is defined as the difference between M_t and the pole mass m_t.

B. Transfer functions

The transfer functions relate the parton transverse momentum, p_T, to the measured jet momentum. They are probability distributions of p/E, the ratio of the magnitude of the jet momentum p to the parent effective parton energy E, parametrized as a function of the transverse momentum of the parent effective parton (described in the previous section). We construct our transfer functions using $t\bar{t} \rightarrow$ lepton + jets MC events in a wide range of top quark masses, requiring the same selection cuts as described earlier. In this sample, the parton is matched to

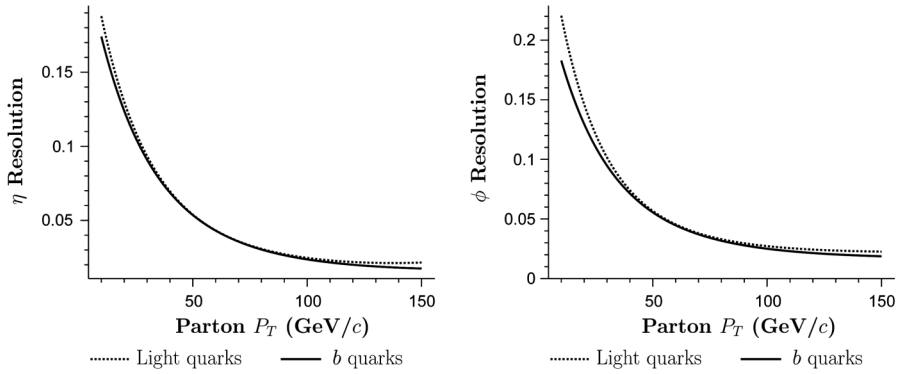

FIG. 5 (color online). Angular resolution in η (left) and ϕ (right) as a function of parton p_T. The dashed line indicates the resolution for light quarks, and the solid line for b quarks.

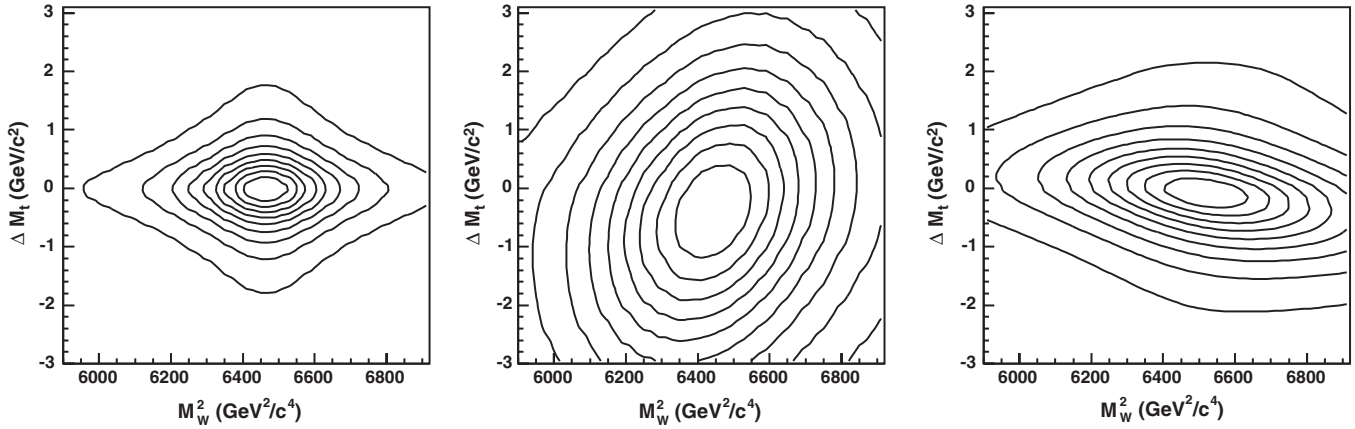

FIG. 6. Contour plots of the propagators in M_W^2 and ΔM_t. Left: Breit-Wigner propagator, for comparison. Center: Sample effective propagator on the hadronic side of the event. Right: Sample effective propagator on the leptonic side of the event.

the simulated jets, p/E distributions are created in bins of the parent parton p_T, and then these distributions are fit with a p_T-parametrized function. The function is constructed using Johnson curves [26], which allow us to fit a variety of non-Gaussian shapes. These curves are parametrized by quantities calculated from the transfer function distributions themselves: mean (μ), standard deviation (σ), skewness (s), and kurtosis (k), which, in turn, smoothly depend on the parton p_T. We extrapolate the fitted transfer functions for momenta that are below the cutoff value imposed in the sample. This extrapolation ensures that the transfer functions are correctly normalized, as it accounts for jets that do not appear in our sample due to selection cuts. Separate transfer functions are cre-

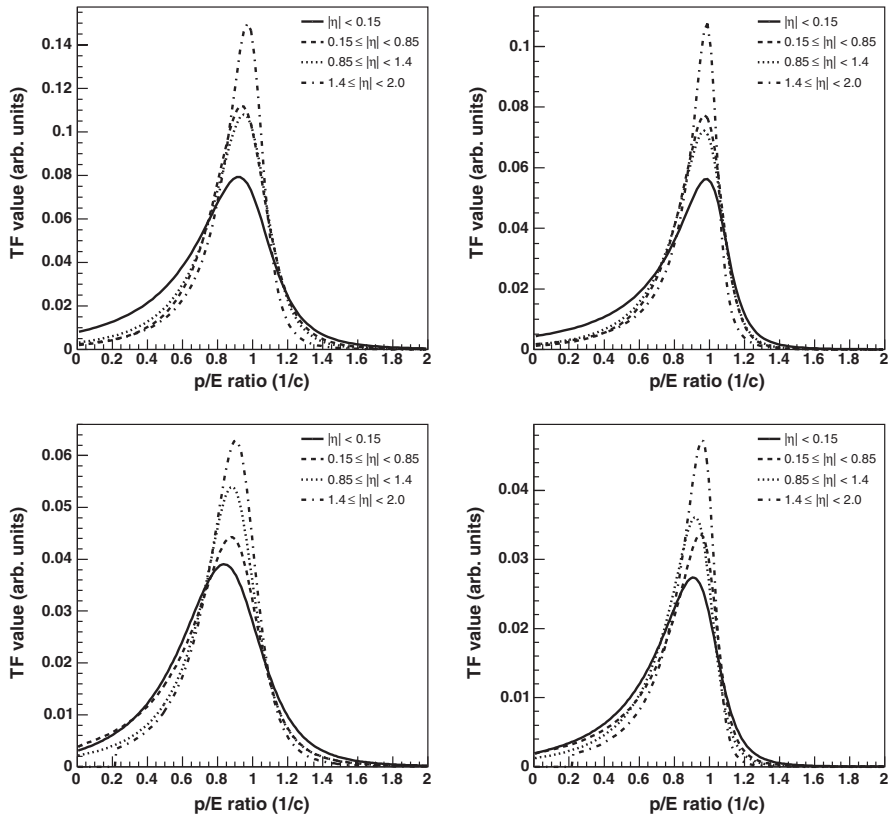

FIG. 7. Sample fitted transfer functions for light and b quarks in η bins. Transfer functions are shown for light quarks with parton $P_T = 40$ and 70 GeV/c (top left and right, respectively), and for b quarks with parton $P_T = 40$ and 70 GeV/c (bottom left and right, respectively).

ated for four different η regions of the detector, as well as for b quarks and light quarks. Figure 7 shows transfer function examples for light and b quarks for several different parton p_T values and η bins.

C. Normalization and acceptance

The normalization factor $N(m_t)$ in Eq. (2) is obtained by integrating the Kleiss-Stirling matrix element [6] together with the PDFs and the flux factor over the phase space formed by the two initial and the six final-state particles. The resulting cross section as compared to the $t\bar{t}$ cross section in HERWIG is shown in Fig. 8. We do not expect perfect agreement due to the absence of radiation in our code.

The resulting normalization is then corrected by a small additional factor to account for the difference between the effective propagators and Breit-Wigners. The normalization correction is calculated as follows. We split the matrix element into two parts: $|M(\vec{x})|^2 = \Gamma_{\text{tree}}(\vec{x})|M(\vec{x})^*|^2$, where $\vec{x}$ completely specifies the phase space point, $\Gamma_{\text{tree}}(\vec{x})$ is the product of the four Breit-Wigners, and $|M(\vec{x})^*|^2$ is the rest of the matrix element. Using this notation, the tree-level normalization is $\int F(\vec{x})\Gamma_{\text{tree}}(\vec{x})|M(\vec{x})^*|^2 d\vec{x}$, where $F(\vec{x})$ is the remaining term in the cross section (flux factor and structure functions). The correct normalization with the effective propagators is instead

$$\int F(\vec{x}_{\text{eff}})\Gamma_{\text{eff}}(\vec{x}_{\text{eff}})|M(\vec{x}_{\text{eff}})^*|^2 d\vec{x}_{\text{eff}}, \tag{5}$$

where $\vec{x}_{\text{eff}}$ specifies the kinematic configuration of the effective partons. This quantity can be rewritten as

$$\int \frac{F(\vec{x}_{\text{eff}})\Gamma_{\text{eff}}(\vec{x}_{\text{eff}})|M(\vec{x}_{\text{eff}})^*|^2 d\vec{x}_{\text{eff}}}{F(\vec{x})\Gamma_{\text{tree}}(\vec{x})|M(\vec{x})^*|^2 d\vec{x}} F(\vec{x})\Gamma_{\text{tree}}(\vec{x})|M(\vec{x})^*|^2 d\vec{x}. \tag{6}$$

From this point forward we proceed as if there is a one-to-one correspondence between points in $\vec{x}$ and $\vec{x}_{\text{eff}}$ [27]. By construction, the propagators play the role of densities in their corresponding spaces. Therefore, $\Gamma_{\text{eff}}(\vec{x}_{\text{eff}})d\vec{x}_{\text{eff}} = \Gamma_{\text{tree}}(\vec{x})d\vec{x}$, and we need only to calculate

$$\int \frac{F(\vec{x}_{\text{eff}})|M(\vec{x}_{\text{eff}})^*|^2}{F(\vec{x})|M(\vec{x})^*|^2} F(\vec{x})\Gamma_{\text{tree}}(\vec{x})|M(\vec{x})^*|^2 d\vec{x}. \tag{7}$$

This quantity is the average value of

$$\frac{F(\vec{x}_{\text{eff}})|M(\vec{x}_{\text{eff}})^*|^2}{F(\vec{x})|M(\vec{x})^*|^2}, \tag{8}$$

calculated over the tree-level MC events, times the cross section. The resulting correction factor is plotted in Fig. 8 as a function of the top quark mass.

The acceptance $A(m_t, \text{JES})$ is obtained from $t\bar{t}$ MC events in which parton angles are randomized to simulate the small angular resolution uncertainty of the detector, and parton momenta are smeared according to our transfer functions to mimic the jet momenta that would have been measured in the detector. The kinematic distributions for the smeared events are similar to those of fully simulated events. We do this for all the values of the top quark mass and JES over which the likelihood function is defined, and then calculate the acceptance at each m_t and JES value to be the fraction of these MC events that pass our selection cuts. The advantage of this approach as opposed to using fully simulated MC events is that the jet-parton association is exact, and events with incorrect jet-parton association can be excluded from the efficiency calculations. Our probability model describes tree-level signal events with the correct set of jets; therefore, we do not use fully simulated events, which include effects not accounted for in our model, such as gluon radiation. The transfer functions are normalized with respect to all jet momenta, not just those which pass the cuts. By building an acceptance function from events smeared according to our transfer functions, we directly normalize our likelihood. Furthermore, we can generate our acceptance from a much larger sample of events because we avoid the computing intensive steps of event simulation and reconstruction, while reducing statistical fluctuations in the resulting curve. Figure 9 shows the 2-D acceptance as a function of m_t and JES.

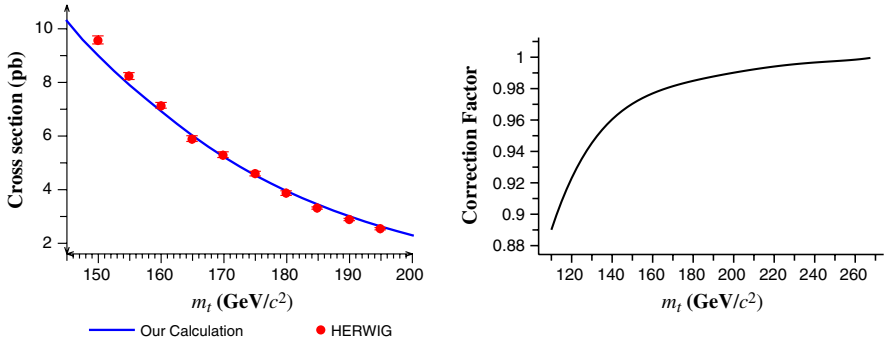

FIG. 8 (color online). Left: Cross section obtained from our normalization calculation as a function of m_t compared with the cross section used in HERWIG. Right: Normalization correction factor due to effective propagators as a function of m_t.

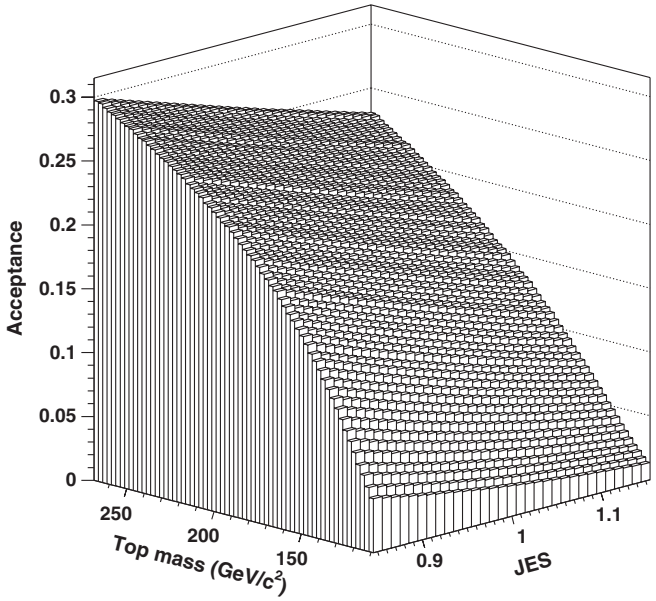

FIG. 9. Acceptance used in Eq. (2) as a function of m_t and JES.

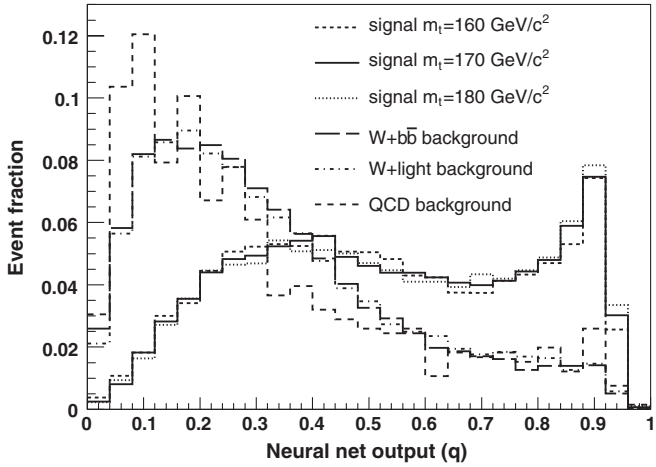

FIG. 10. The distributions of our neural network discriminant variable for signal and background MC events. The peaks on the right are from $t\bar{t}$ signal events at three top masses. The peaks on the left are from various types of backgrounds.

V. BACKGROUND DISCRIMINATION AND FINAL LIKELIHOOD

Our integration method calculates the likelihood for an event assuming the $t\bar{t}$ hypothesis, hence we use a neural network approach to discriminate against background events. The neural network uses ten inputs: seven variables describing the kinematics of the event (the p_T for the four leading jets, the lepton E_T, $\not\!\!E_T$, and H_T, the scalar sum of these quantities), and three variables describing the topology of the event. The three topological variables are aplanarity, D_R, and H_{TZ}. The aplanarity is defined as $(3/2)Q_1$, where Q_1 is the smallest eigenvalue of the normalized momentum tensor $\Theta_{ab} = \sum_i p_a^i p_b^i / \sum_i |\vec{p}_i|^2$, where the indices a and b run over the three axes x, y, and z, the index i runs over the four jets and charged lepton, and $\vec{p}_i$ is the three-momentum of a given particle. The variable $D_R = \Delta R_{ij}^{\min} \cdot \min(p_z^{(i,j)})/p_T^{\ell}$, where $\Delta R_{ij}^{\min}$ is the smallest ΔR between any pair of jets, $\min(p_z^{(i,j)})$ is the smaller of the two p_z values for the two jets in that pair, and p_T^{ℓ} is the transverse momentum of the charged lepton. H_{TZ} is a ratio of scalar sums of transverse and longitudinal momenta; the numerator contains all jets except the leading jet, and the denominator sums all jets, the charged lepton, and the neutrino. The smaller $|p_z^{\nu}|$ solution given by the kinematic equation for the leptonic W boson decay (assuming $M_W = 80.4\ \mathrm{GeV}/c^2$) is taken. The ten variables are summarized in Table II. To construct the neural network, we use the JETNET neural network package, version 3.5 [28].

The neural network is trained to separate $t\bar{t}$ events with a mass of $170\ \mathrm{GeV}/c^2$ from $W + b\bar{b}$ background; we then cross-check the neural network with other signal masses and background types to make sure that the output shape is not dependent on the signal mass present. Figure 10 shows the neural network output, q, for a variety of different samples. We compute the background fraction for each observed event as $f_{\mathrm{bg}}(q) = B(q)/[B(q) + S(q)]$, where the background distribution $B(q)$, obtained by adding each type of background with its own weight, and signal distribution $S(q)$ are each normalized to their overall expected fractions.

Our total likelihood from all events will naturally contain likelihoods from signal events and background events.

TABLE II. Variables included in the neural network discriminant: the first seven are kinematic variables, the last three are topological variables.

Variable	Definition
p_T^i	p_T of each of the 4 leading jets
E_T^{ℓ}	Charged lepton E_T (electron) or p_T (muon)
$\not\!\!E_T$	The missing E_T
H_T	Scalar sum of jets and lepton transverse momenta and $\not\!\!E_T$
Aplanarity $= 3/2 \cdot Q_1$	Q_1: smallest eigenvalue of the momentum tensor
$D_R = \Delta R_{ij}^{\min} \cdot \min(p_z^{(i,j)})/p_T^{\ell}$	$\Delta R_{ij}^{\min}$ is the smallest ΔR between any pair of jets
$H_{\mathrm{TZ}} = \sum_{i=2}^{4} \lvert p_T^i \rvert / (\sum_{i=1}^{4} \lvert p_z^i \rvert + \lvert p_z^{\ell} \rvert + \lvert p_z^{\nu} \rvert)$	Ratio of scalar sums of transverse to longitudinal momenta

However, only the signal events will contain meaningful information about m_t. Thus, we want to remove the contribution due to background events from the total likelihood to recover the likelihood from signal events. (Note that there is not a separate matrix element for background processes—the likelihood for all events, signal and background, is calculated under the assumption that the event is a $t\bar{t}$ signal event.) Consequently, we compute from Monte Carlo simulation the average likelihood for background events and subtract out the expected contribution due to background events from the total likelihood:

$$\log L_{\mathrm{mod}}(m_t, \mathrm{JES}) = \sum_{i \in \mathrm{events}} [\log L(\vec{y}_i | m_t, \mathrm{JES})] - n_{\mathrm{bg}} \log \bar{L}_{\mathrm{bg}}(m_t, \mathrm{JES}), \quad (9)$$

where L_{mod} is the modified total likelihood for a given set of events, $L(\vec{y}_i|m_t, \mathrm{JES})$ is the likelihood for an individual event, n_{bg} the expected number of background events, and $\bar{L}_{\mathrm{bg}}(m_t, \mathrm{JES})$ is the average likelihood for a background event as computed in Monte Carlo simulation. This calculation is performed separately for 1-tag and >1-tag events, as the background fractions and $\bar{L}_{\mathrm{bg}}(m_t, \mathrm{JES})$ are different for the two subsamples.

We can rewrite Eq. (9) in terms of the individual per-event background fraction to obtain our final modified likelihood L_{mod}:

$$\log L_{\mathrm{mod}}(m_t, \mathrm{JES}) = \sum_{i \in \mathrm{events}} [\log L(\vec{y}_i | m_t, \mathrm{JES}) - f_{\mathrm{bg}}(q_i) \log \bar{L}_{\mathrm{bg}}(m_t, \mathrm{JES})], \quad (10)$$

where $f_{\mathrm{bg}}(q_i)$ is the background fraction given the discriminant variable q_i for a given event. Equations (9) and (10) are equivalent if the number of background events in the data is equal to the expected background contribution. However, the advantage of using Eq. (10) is that if there are more or fewer background-like events in our data than expected, the average value of $f_{\mathrm{bg}}(q_i)$ will be correspondingly higher or lower, thus compensating for the difference.

There is another class of events not well modeled by our signal likelihood integration or handled by the background subtraction above, which we call "bad signal" events. These are $t\bar{t}$ signal events in which the four observed jets and/or lepton are not directly produced from the $t\bar{t}$ decay. These events exist due to a variety of causes (extra jets from gluon radiation, $t\bar{t}$ events where both W bosons decay leptonically or hadronically, $W \rightarrow \tau\nu$ decay, etc.) and comprise roughly 35% of our total signal. For a signal mass of 172 GeV/c^2, 36.2% of the single-tag and 30.9% of the >1-tag events fall into the "bad signal" category.

We observe that the peaks of the likelihood curves for these "bad signal" events tend to be generally lower than the peaks for well-behaved $t\bar{t}$ events. Figure 11 shows the distribution of the peak value of the likelihood curves for "good signal," "bad signal," and background events. We adopt a cut on the peak value of the likelihood of 6, which retains only the bins dominated by "good signal." Table III shows the efficiency of this cut for "good signal" events, "bad signal" events, and background events for $m_t = 172$ GeV/c^2. With this cut we remove ~22% of the "bad signal" events and ~29% of the background events while retaining ~95% of "good signal" events. While this cut reduces the size of our sample, the overall resolution is significantly improved due to the improved validity of our assumptions about the sample.

Our calculation gives us a 2-dimensional joint likelihood as a function of m_t and JES. We treat the JES as a nuisance parameter and eliminate it using the profile likelihood, i.e., we take the maximum value of the likelihood along the JES axis for each m_t value. That is:

$$L_{\mathrm{prof}}(m_t) = \max_{j \in \mathrm{JES}} L(m_t, j). \quad (11)$$

This gives us a 1-D likelihood curve in m_t only. We then follow the normal procedure of taking the position of the maximum likelihood as our reconstructed mass and de-

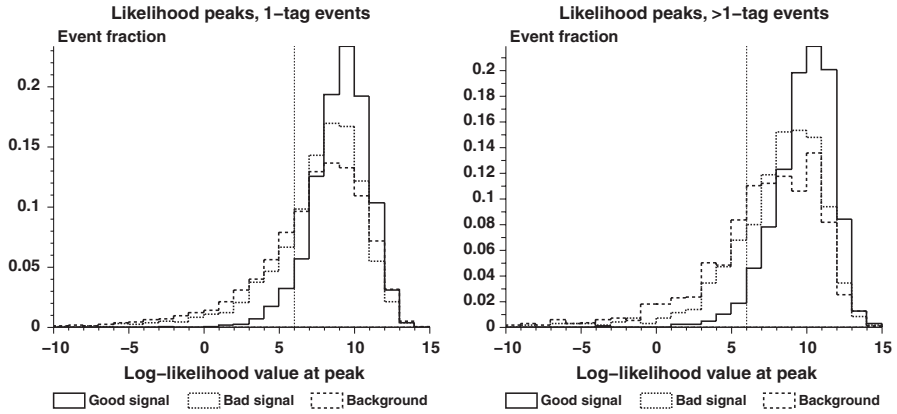

FIG. 11. Distributions of the peak value of the log-likelihood for MC events, divided into "good signal," "bad signal," and background events. Left: 1-tag events, right: multiple-tag events. The vertical lines indicate where the likelihood cut is applied.

TABLE III. Efficiency of the likelihood cut at a value of 6 for $m_t = 172$ GeV/c^2. The uncertainties shown are the binomial uncertainties on the cut, summed appropriately across the different background types for the background.

Type of event	1-tag	>1-tag
Good signal	93.6% ± 0.4%	96.9% ± 0.4%
Bad signal	76.8% ± 0.9%	77.5% ± 1.5%
Background	70.4% ± 0.5%	68.9% ± 1.3%

scending 1/2 unit of log-likelihood from the peak to determine the estimated uncertainty. Because of imperfections in our model, these quantities need to be calibrated in order to obtain a final measured mass and uncertainty.

VI. TEST OF THE METHOD AND CALIBRATION

We test our method using MC samples of fully simulated and reconstructed $t\bar{t}$ events and the background samples described in Sec. III. We construct pseudoexperiments (PEs) from the MC samples with an average total number of events equal to the number observed in the data. As shown in Table I we observe 371 events, of which 70.3 ± 16.5 are expected to be background. After applying the likelihood cut efficiencies for signal and background simulated events, we expect a total of 303 events, which is the number of events that we use in our PEs. The number of each type of event (signal and each background type) is Poisson-fluctuated about its expected contribution to the total. We perform 2000 PEs for each signal top quark mass value and compute the resulting average reconstructed mass, bias, expected statistical uncertainty, and pull width. Figure 12 shows the reconstructed mass, bias, and pull width versus the input top quark mass, where the bias is defined as the difference between the true mass m_{true} and the reconstructed mass m_{rec} and the pull width is the width of the distribution of $(m_{\text{rec}} - m_{\text{true}})/(\sigma_m)_{\text{rec}}$ in individual PEs, where $(\sigma_m)_{\text{rec}}$ is the estimated uncertainty. The output mass is a linear function of the input mass with a slope very close to 1; the mass bias and the pull width are independent of the input top quark mass. The nonzero bias and nonunit pull width are due to the presence of events not modeled in our effective propagator model ("bad signal" events and background) in our analysis; if we run PEs on "good signal" events only, we obtain a bias and average pull width consistent with 0 and 1, respectively.

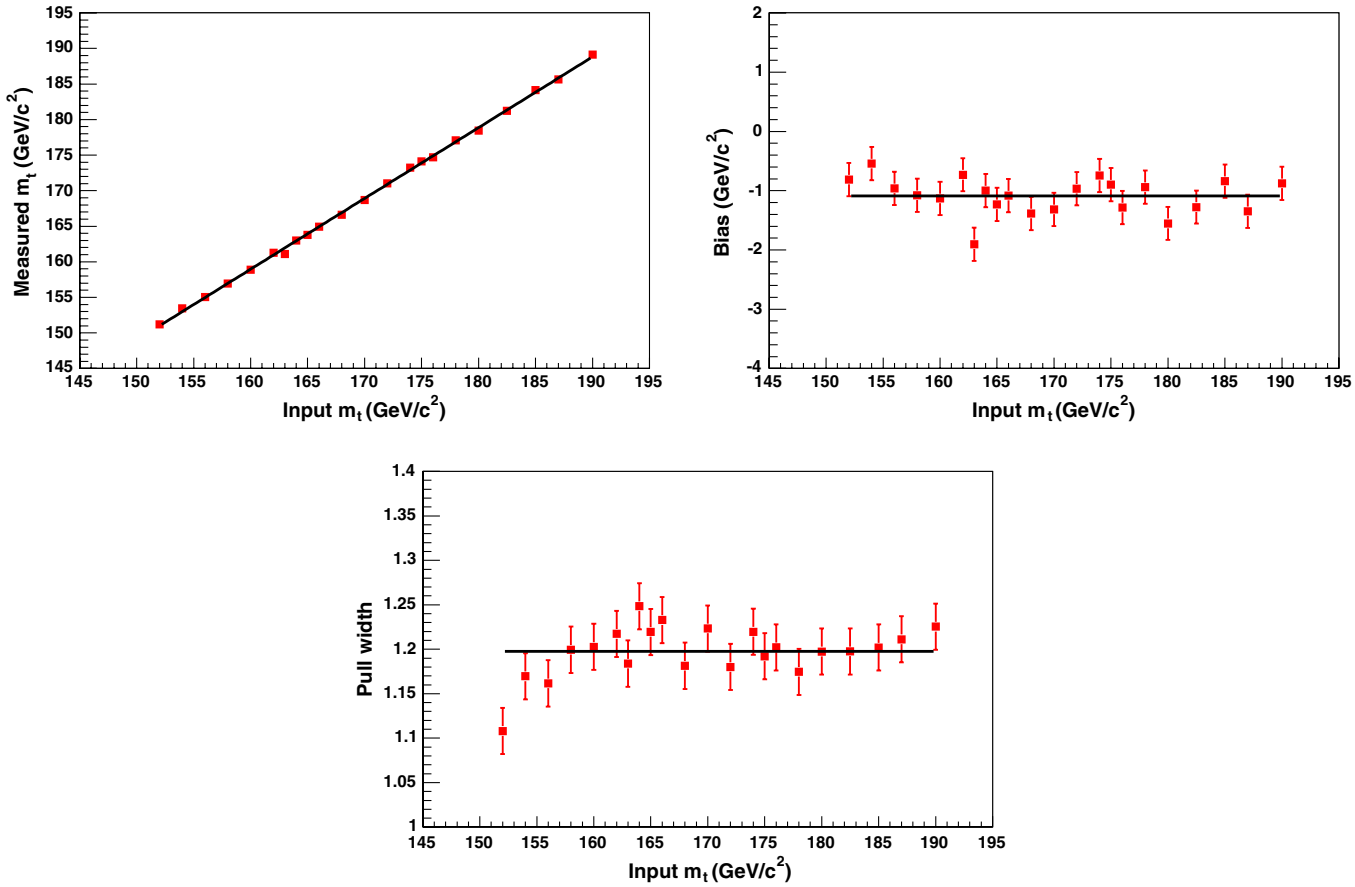

FIG. 12 (color online). Pseudoexperiment results using fully simulated signal and background events after applying a likelihood cut, with a mean of 303 events for each PE. For these samples, JES is fixed at its nominal value of 1. Top left: reconstructed vs input top quark mass; top right: bias vs input top quark mass; bottom: pull width vs input top quark mass.

We use the observed slope, bias, and pull width to calibrate our method. Specifically, the reconstructed mass is calibrated by correcting for the measured bias and slope, and the estimated uncertainty is calibrated by correcting for the measured pull width and slope. We perform our calibrations in terms of $\Delta m_t \equiv m_t - 172\ \mathrm{GeV}/c^2$; our overall calibration formulae to obtain a calibrated mass Δm_{cal} and mass uncertainty $(\sigma_m)_{\mathrm{cal}}$ in terms of the observed mass Δm_{obs} and uncertainty $(\sigma_m)_{\mathrm{obs}}$ are

$$\Delta m_{\mathrm{cal}} = (\Delta m_{\mathrm{obs}} - c_2)/c_1, \tag{12}$$

$$(\sigma_m)_{\mathrm{cal}} = (\sigma_m)_{\mathrm{obs}} \times c_3/c_1, \tag{13}$$

where c_1, c_2, and c_3 are the slope in the upper-left plot, the constant in the upper-right plot, and the constant in the bottom plot of Fig. 12, respectively. Using the fits shown in these plots, we obtain $c_1 = 0.995 \pm 0.006$, $c_2 = -1.09 \pm 0.06\ \mathrm{GeV}/c^2$, and $c_3 = 1.20 \pm 0.01$.

The 2-D likelihood method measures JES *in situ* in the $t\bar{t}$ sample. To ensure that this method correctly handles events where the JES is not necessarily equal to its nominal value, we also check simulated samples where the JES has been shifted from its nominal value of unity. Specifically, we use four different JES shifts: JES = 0.95, 0.97, 1.03, and 1.05, to obtain a calibration for our JES measurement in the same way that we calibrate our m_t measurement above. Figure 13 shows the reconstructed JES, JES bias, and JES pull width versus the input JES for $m_t = 170\ \mathrm{GeV}/c^2$. The nonunity pull width for JES is due to the same origin as the nonunity pull width for the top mass. We use these results to obtain our calibration for the reconstructed JES. We perform our calibrations in terms of $\Delta(\mathrm{JES}) \equiv \mathrm{JES} - 1$, yielding the final formulae for our calibrated $\Delta(\mathrm{JES})$, $\Delta(\mathrm{JES})_{\mathrm{cal}}$, and JES uncertainty $(\sigma_{\mathrm{JES}})_{\mathrm{cal}}$ in terms of the observed value, $\Delta(\mathrm{JES})_{\mathrm{obs}}$, and uncertainty $(\sigma_{\mathrm{JES}})_{\mathrm{obs}}$:

$$\Delta(\mathrm{JES})_{\mathrm{cal}} = (\Delta(\mathrm{JES})_{\mathrm{obs}} - c_5)/c_4 \tag{14}$$

$$(\sigma_{\mathrm{JES}})_{\mathrm{cal}} = (\sigma_{\mathrm{JES}})_{\mathrm{obs}} \times c_6/c_4, \tag{15}$$

where c_4, c_5, and c_6 are the slope in the upper-left plot, the constant in the upper-right plot, and the constant in the bottom plot of Fig. 13, respectively. Using these results, we obtain $c_4 = 1.03 \pm 0.04$, $c_5 = 0.0003 \pm 0.0013$, and $c_6 = 1.17 \pm 0.01$.

Since the m_t and JES calibration parameters are derived for JES fixed at 1 and m_t fixed at $170\ \mathrm{GeV}/c^2$, respectively, we also need to ensure that they do not vary for different values of m_t and JES. Figure 14 shows the results

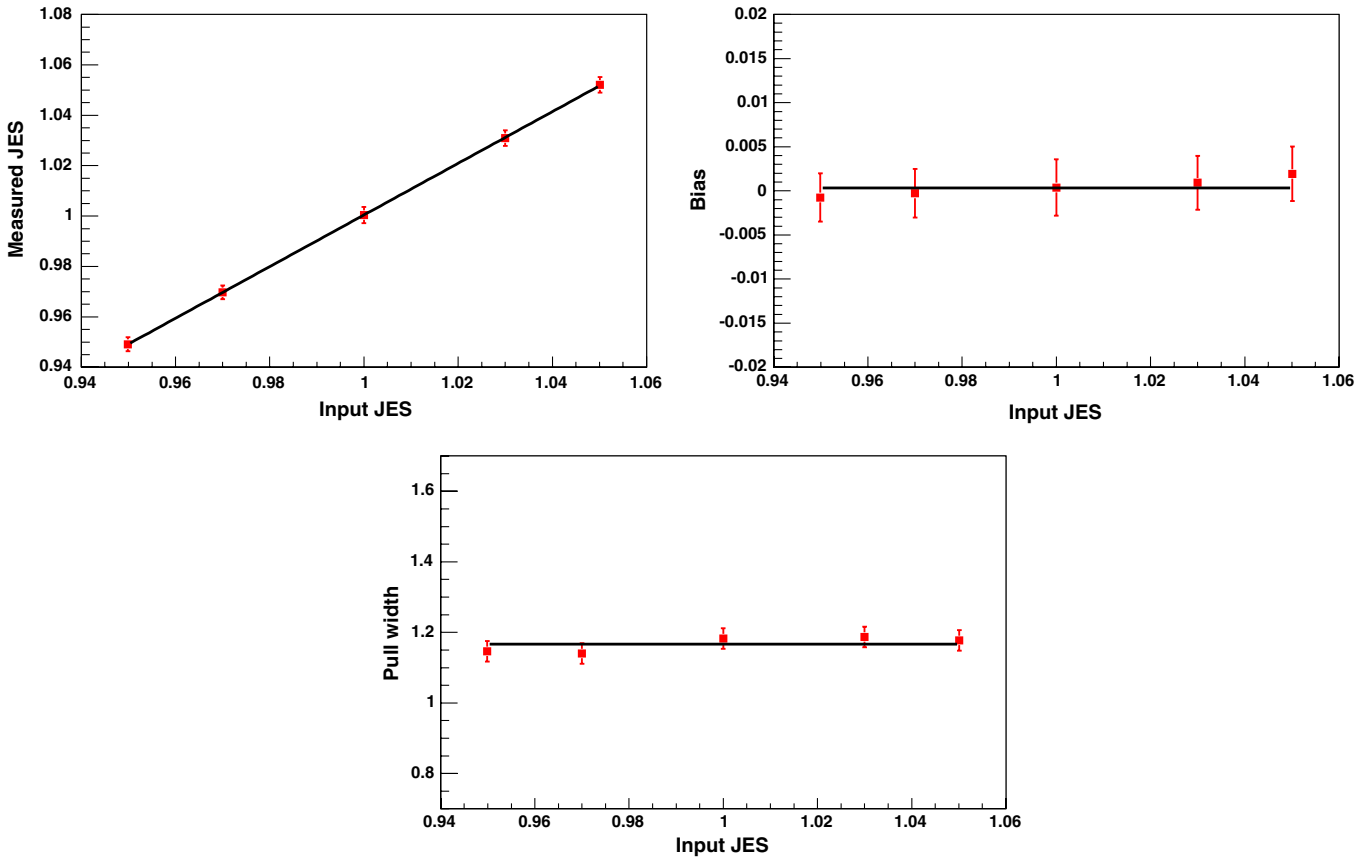

FIG. 13 (color online). JES pseudoexperiment results using fully simulated signal and background events after applying a likelihood cut, with a mean of 303 events for each PE. The top quark mass here is fixed at $m_t = 170\ \mathrm{GeV}/c^2$. Top left: reconstructed vs input JES; top right: JES bias vs input JES; bottom: JES pull width vs input JES.

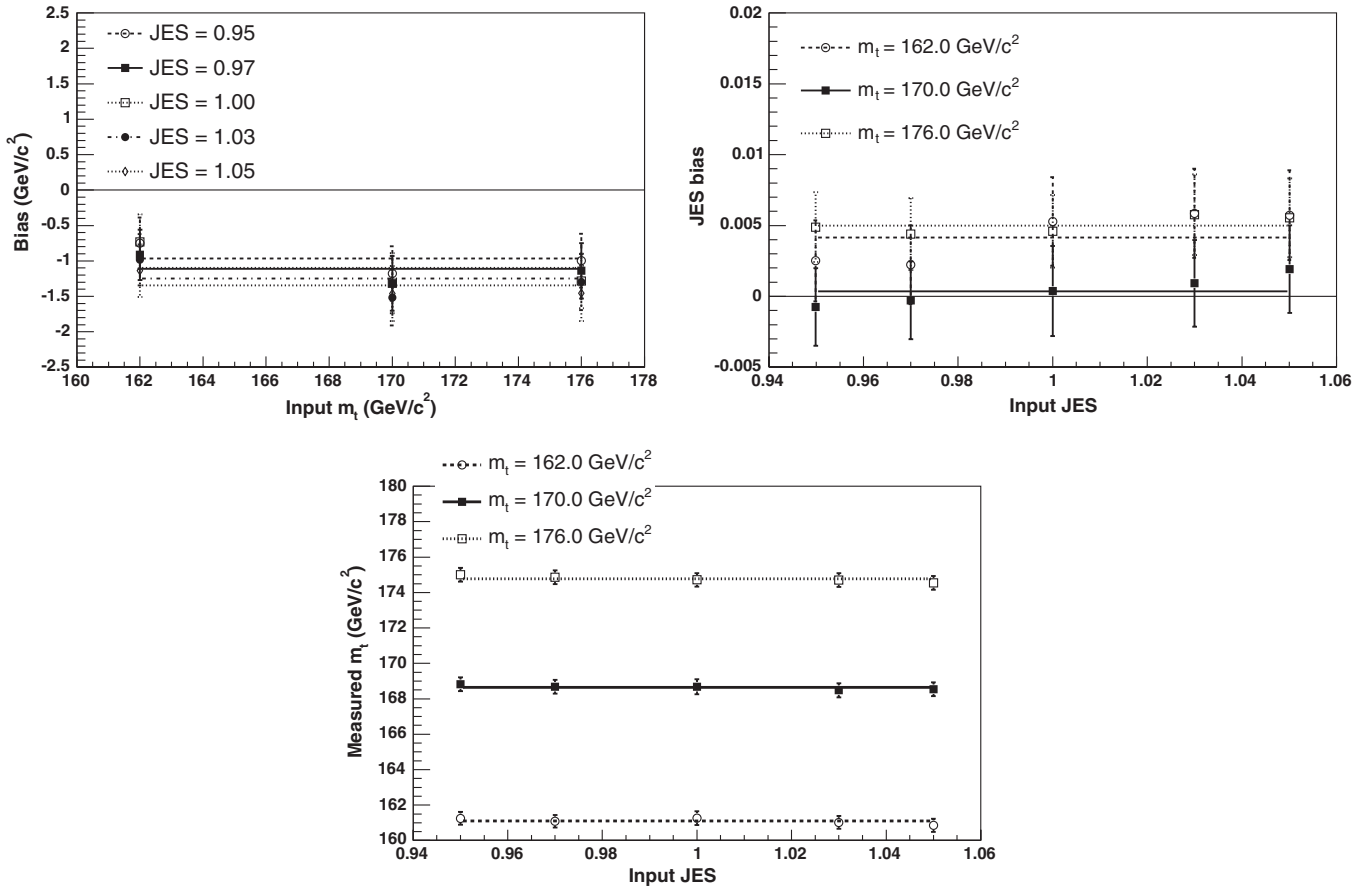

FIG. 14. Results of studying samples with shifted JES values. Top left: Mass bias vs input top quark mass at the five different JES points; top right: JES bias vs input JES at the three different mass points; bottom: reconstructed top quark mass vs input JES for the three different top quark masses.

of these studies. We note that the JES and m_t slope and bias do not noticeably change for different m_t and JES inputs. The plot on the bottom also shows that the reconstructed top quark mass is very stable with respect to the input JES, showing that our procedure of independent calibration of the two variables is valid.

VII. SYSTEMATIC UNCERTAINTIES

We discuss the systematic uncertainties on our measurement in this section. Most systematics are evaluated using a general procedure where we shift a given quantity by $\pm 1\sigma$ in the signal MC sample and/or in the background samples, perform PEs to measure a top quark mass on the shifted sample, and use the resulting shift in the measured top quark mass as our systematic uncertainty. In this paper, we have rounded all of the final systematic uncertainties to a precision of 0.1 GeV$/c^2$; although some systematics are known to a higher precision than this, some are not.

(i) *Calibration:* In calibrating our final result, we use the bias and slope constants c_1, c_2, and c_3 as described in Sec. IV. The uncertainty on these constants is a source of systematic uncertainty in our measurement. The uncertainty in c_1 is the major source of our final quoted uncertainty of 0.1 GeV$/c^2$.

(ii) *Residual JES:* Although the 2-D measurement is designed to capture any changes in the JES, we assume a constant factor for the jet energy scale, whereas the jet energy systematic uncertainties depend on the jet p_T and η. Furthermore, the JES uncertainties are composed of the sum of several different potential sources, each of which may vary differently. To evaluate potential systematic uncertainties due to this assumption, we shift the jet energies by 1 standard deviation for each source of systematic uncertainty (corrections for relative response of different sections of the calorimeter, the absolute corrections in cone with $\Delta R = 0.4$, out-of-cone correction details, and other minor sources as described in Ref. [29]). We perform these tests shifting only the signal, and also shifting the signal together with the $W + b\bar{b}$ background, and take the greater of the resulting differences. The resulting shifts are added in quadrature to obtain our residual JES systematic uncertainty of 0.5 GeV$/c^2$.

(iii) *b-JES:* We have assumed that the JES is the same for all jets. However, there is an additional uncertainty arising from relative differences between b- and light-quark jets. (Note that the jet systematic uncertainties are predominantly determined using light jets.) We identify three sources of uncertainty: one due to the uncertainty in the semileptonic decay ratio, which we estimate by varying this ratio by $\pm 1\sigma$; one due to the uncertainty in the b-fragmentation modeling, which we evaluate by varying the parameters used in the Bowler fragmentation model [30] in the PYTHIA Monte Carlo generator, using two different sets of parameters derived from SLD and LEP results [31]; and one due to uncertainty in the calorimeter response for b-jets compared to light-quark jets. Because the calorimeter response is determined in light-jet samples, the different charged particle fraction and momentum spectrum in b-jets could result in a different response. We evaluate this uncertainty by checking the effect of the calorimeter corrections in simulated light jets and b-jets separately. Then we propagate this difference in the response by shifting the E_T of jets identified as b-jets in the $t\bar{t}$ Monte Carlo sample. The three corrections to the b-jet energy scale yield uncertainties of 0.1 GeV/c^2, 0.3 GeV/c^2, and 0.1 GeV/c^2, respectively, for an overall uncertainty of 0.3 GeV/c^2.

(iv) *Generator:* We evaluate a systematic due to the MC generator used by comparing the results from HERWIG and PYTHIA $t\bar{t}$ samples. We take the resulting difference of 0.6 GeV/c^2 as our systematic uncertainty. There is also a potential systematic uncertainty for color reconnection effects not included here [32]; current studies suggest that these may not significantly increase our total systematics.

(v) *ISR and FSR:* Systematic errors due to initial-state radiation (ISR) and final-state radiation (FSR), where additional gluons are radiated, are evaluated using MC samples. A control sample of Drell-Yan events allows us to compare the dilepton invariant mass spectrum in data and MC and estimate the uncertainty on the parameters controlling the radiation [29]. Those parameters have been varied by the estimated uncertainty to study the effect on the top mass measurement. In this case the uncertainty on the measured top mass shift is larger than the shift itself, so we use the uncertainty of 0.3 GeV/c^2 as our quoted uncertainty.

(vi) *PDFs:* We evaluate the systematic uncertainty due to the parton distribution functions (PDFs) used in the matrix element integration by comparing different PDF sets (CTEQ5L [24] and MRST72 [33]), varying α_s, and varying the eigenvectors of the CTEQ6M PDFs. The final uncertainty is defined by the sum of the eigenvector uncertainties in quadrature and the difference from the α_s variation. The CTEQ-MRST difference in our case is negligible. The result is an overall uncertainty of 0.4 GeV/c^2.

(vii) *Background:* There are several uncertainties associated with our background subtraction. First is the uncertainty due to uncertainty on the overall background fraction. The second source is the uncertainty in the background composition, which we assess by setting the background to, in turn, 100% $W + b\bar{b}$, $W + c\bar{c}/c$, $W +$ light, or QCD background and taking the largest resulting shift as our uncertainty. Third, the uncertainty associated with our average background likelihood $\bar{L}_{\mathrm{bg}}(m_t, \mathrm{JES})$ as described in Sec. V; to evaluate this uncertainty, we divide the sample into two disjoint subsamples (one with only electrons, and one with only muons), build the average background likelihood curve from one subsample, and measure the top quark mass using the other subsample. Finally, we account for uncertainties due to the Q^2 scale used by the background MC generator. The resulting systematic uncertainties are 0.3 GeV/c^2, 0.4 GeV/c^2, 0.3 GeV/c^2, and 0.2 GeV/c^2, respectively.

(viii) *Lepton p_T*: To account for the 1% uncertainty on the measured lepton p_T, we apply our method to samples where the lepton p_T has been shifted by this amount, resulting in an uncertainty on the top quark mass of 0.1 GeV/c^2.

(ix) *Permutation weighting:* We account for a potential systematic for the tagging probabilities used to weight our permutations (the w_i factors in Eq. (2)), since these are derived from fits to the tagging probabilities measured in data. We estimate that the predominant source of uncertainty in this estimate is the ratio of charm tags to b-tags, which is nominally 22%. We vary this by its relative uncertainty of 15% and measure the resulting difference, which is negligible.

(x) *Pileup:* We consider two sources of uncertainty due to multiple $p\bar{p}$ interactions. First, we consider the fact that the number of interactions in our Monte Carlo samples is not equal to the number observed in the data. To estimate this effect, we divide our Monte Carlo samples into subsamples with differing numbers of interactions in the event, examine the slope of the resulting measured top quark mass as a function of the number of interactions, and multiply this by the difference in the number of interactions between Monte Carlo events and data events. Second, we consider the modeling of the additional interactions in an event. Our current model is derived from minimum bias events, so we consider the possibility that it does not correctly model $t\bar{t}$ events. For this purpose, we compare the

TABLE IV. Total list of systematic uncertainties.

Systematic source	Systematic uncertainty (GeV/c^2)
Calibration	0.1
Residual JES	0.5
b-JES	0.3
MC generator	0.6
ISR and FSR	0.3
PDFs	0.4
Background: fraction	0.3
Background: composition	0.4
Background: average shape	0.3
Background: Q^2	0.2
Lepton p_T	0.1
Pileup	0.2
Gluon fraction	0.3
Total	1.2

observed jet response as a function of the number of vertices in $t\bar{t}$ Monte Carlo events and minimum bias data and use the resulting difference to obtain a systematic uncertainty. We take the larger of these two sources, 0.2 GeV/c^2, as our systematic uncertainty.

Gluon fraction: HERWIG and PYTHIA are both leading-order MC generators, so $t\bar{t}$ events in these samples are approximately 95% produced from $q\bar{q}$ annihilation and 5% produced from gg fusion. However, NLO expectations are closer to $(15 \pm 5)\%gg$ production. To check for a potential systematic due to this effect, we run PEs where $q\bar{q}$ and gg events are reweighted so that the $q\bar{q}$ weights sum to 0.80 and the gg events to 0.20 (using the maximal gg percentage to be conservative) and use the resulting shift of 0.3 GeV/c^2 as our uncertainty.

Table IV summarizes our final list of systematic uncertainties.

VIII. RESULTS

In the data we find a total of 318 events which pass all of our selection requirements (including the likelihood peak value cut), of which 237 have exactly 1 tag and 81 have more than 1 tag. We combine the likelihoods for the 1-tag and >1-tag subsamples using the formula described in Eq. (10) and then combine the two subsamples. After obtaining this total likelihood, we use the profile likelihood method introduced in Sec. V to extract a top quark mass value. That mass value is then corrected using the calibration procedure to obtain a mass value of 172.7 ± 1.8 GeV/c^2. The left plot in Fig. 15 shows the resulting 2-D likelihood contours after calibration for 1-σ, 2-σ, and 3-σ uncertainties, assuming that they have Gaussian distributions.

To validate the likelihood cut used in our procedure, we compare distributions of the event peak likelihoods in data and MC events. The K-S confidence level for these two distributions is 93.8%, indicating a very good agreement between the data and MC simulations.

This result combines the statistical uncertainty and the uncertainty due to JES. To separate these two contributions, we fix the JES value to be 1.0 and evaluate the uncertainty in the resulting 1-D likelihood as a function of m_t. This yields an uncertainty of 1.2 GeV/c^2. We conclude that the remaining uncertainty of 1.3 GeV/c^2 is due to the JES. The expected statistical + JES uncertainty from MC events at a top quark mass of 172 GeV/c^2 peaks at 1.8 GeV/c^2, in good agreement with the measured uncertainty in the observed event sample of 1.8 GeV/c^2; 50% of pseudoexperiments show a smaller uncertainty than that measured in the data. The distribution of the expected uncertainties is shown in Fig. 16. The additional systematic uncertainty on the measured top mass discussed in Sec. VII is 1.2 GeV/c^2, yielding a final result of:

$$m_t = 172.7 \pm 1.2(\text{stat}) \pm 1.3(\text{JES}) \pm 1.2(\text{syst}) \text{ GeV}/c^2.$$

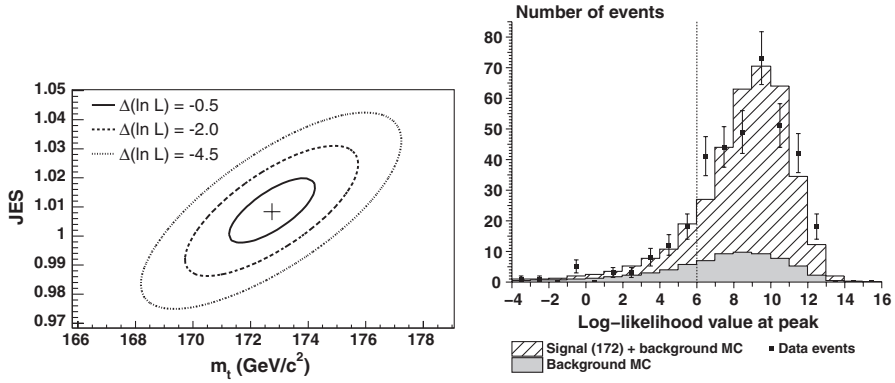

FIG. 15. Left: Measured 2-D likelihood on the data events. The plot shows the contours corresponding to a 1-σ, 2-σ, and 3-σ uncertainty (assuming Gaussian behavior) in our measurement. The calibration derived from MC events has been applied to both axes. The marker shows the point of maximum likelihood. Right: Likelihood peak position of the individual likelihood curves for data and MC events. The dashed line indicates the likelihood cut of 6 employed.

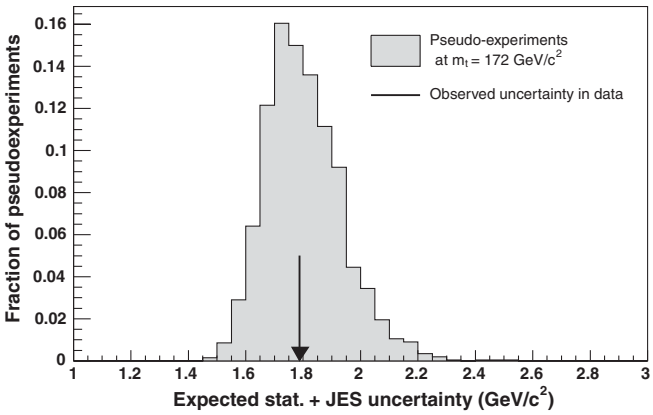

FIG. 16. Expected statistical uncertainty (including uncertainty due to JES) on the top mass from the 2-D profile likelihood method, derived from MC events with $m_t = 172$ GeV/c^2. The black arrow indicates the uncertainty in the data measurement. All uncertainties have been scaled by the average pull width of 1.198. They are also corrected by $1/0.995$ to account for a measured response slope slightly different from 1.

From the 2-D likelihood, we can also obtain a JES measurement by using the profile likelihood technique to eliminate the m_t axis and applying the calibration described previously. This yields a measurement of JES $= 1.008 \pm 0.013$, indicating that the JES is well within its expected value. Note that the profile likelihood measurement technique does not impose any prior expectations on our JES value.

IX. CONCLUSION

We have used 1.9 fb^{-1} of data at the Tevatron to measure the mass of the top quark using the lepton + jets topology. Our analysis uses a modified matrix element integration technique. To date, analyses using this technique have made simplifying kinematic assumptions for the purposes of computational tractability. The method described in this paper includes the first attempt to compensate directly for these assumptions. Our measured top quark mass with 318 events passing all our selection criteria is:

$$m_t = 172.7 \pm 1.8(\text{stat} + \text{JES}) \pm 1.2(\text{syst})\ \text{GeV}/c^2$$

or combining statistical and systematic uncertainties (assuming Gaussian behavior)

$$m_t = 172.7 \pm 2.1(\text{total})\ \text{GeV}/c^2.$$

Our model at the moment does not take into account events where a jet from top quark decay is missing or is replaced by a jet from the parton shower. Proper treatment of these ''bad signal'' events should help improve the measurement.

ACKNOWLEDGMENTS

We thank the Fermilab staff and the technical staffs of the participating institutions for their vital contributions. This work was supported by the U.S. Department of Energy and National Science Foundation; the Italian Istituto Nazionale di Fisica Nucleare; the Ministry of Education, Culture, Sports, Science and Technology of Japan; the Natural Sciences and Engineering Research Council of Canada; the National Science Council of the Republic of China; the Swiss National Science Foundation; the A. P. Sloan Foundation; the Bundesministerium für Bildung und Forschung, Germany; the Korean Science and Engineering Foundation and the Korean Research Foundation; the Science and Technology Facilities Council and the Royal Society, UK; the Institut National de Physique Nucleaire et Physique des Particules/CNRS; the Russian Foundation for Basic Research; the Ministerio de Ciencia e Innovación, and Programa Consolider-Ingenio 2010, Spain; the Slovak R&D Agency; and the Academy of Finland.

[1] Tevatron Electroweak Working Group, FERMILAB Report No. FERMILAB-TM-2403-E.
[2] LEP Collaborations and LEP Electroweak Working Group, CERN Report No. CERN-PH-EP/2007-039.
[3] W. M. Yao *et al.* (Particle Data Group), J. Phys. G **33**, 1 (2006).
[4] T. Aaltonen *et al.* (CDF Collaboration), FERMILAB Report No. Fermilab-Pub-08-415-E; V. Abazov *et al.* (D0 Collaboration), Phys. Rev. Lett. **101**, 182001 (2008).
[5] K. Kondo, J. Phys. Soc. Jpn. **57**, 4126 (1988); V. Abazov *et al.* (D0 Collaboration), Nature (London) **429**, 638 (2004).
[6] R. Kleiss and W. J. Stirling, Z. Phys. C **40**, 419 (1988).
[7] D. Acosta *et al.* (CDF Collaboration), Phys. Rev. D **72**, 052003 (2005).
[8] C. S. Hill (CDF Collaboration), Nucl. Instrum. Methods Phys. Res., Sect. A **530**, 1 (2004).
[9] A. Sill (CDF Collaboration), Nucl. Instrum. Methods Phys. Res., Sect. A **447**, 1 (2000).
[10] A. Affolder *et al.* (CDF Collaboration), Nucl. Instrum. Methods Phys. Res., Sect. A **453**, 84 (2000).
[11] A. Affolder *et al.* (CDF Collaboration), Nucl. Instrum. Methods Phys. Res., Sect. A **526**, 249 (2004).
[12] F. Abe *et al.* (CDF Collaboration), Phys. Rev. Lett. **68**,

1104 (1992).
[13] A. Bhatti *et al.* (CDF Collaboration), Nucl. Instrum. Methods Phys. Res., Sect. A **566**, 375 (2006).
[14] A. Abulencia *et al.* (CDF Collaboration), Phys. Rev. D **73**, 092002 (2006).
[15] E. J. Thomson *et al.*, IEEE Trans. Nucl. Sci. **49**, 1063 (2002).
[16] D. Acosta *et al.* (CDF Collaboration), Phys. Rev. D **71**, 052003 (2005).
[17] D. Acosta *et al.* (CDF Collaboration), Phys. Rev. D **71**, 072005 (2005); D. Sherman, Ph.D. thesis, Harvard University, 2007.
[18] T. Sjöstrand, P. Edén, C. Friberg, L. Lönnblad, G. Miu, S. Mrenna, and E. Norrbin, Comput. Phys. Commun. **135**, 238 (2001).
[19] G. Corcella, I. G. Knowles, G. Marchesini, S. Moretti, K. Odagiri, P. Richardson, M. H. Seymour, and B. R. Webber, J. High Energy Phys. 01 (2001) 010.
[20] M. Cacciari, S. Frixione, G. Ridolfi, M. L. Mangano, and P. Nason, J. High Energy Phys. 04 (2004) 068; N. Kidonakis and R. Vogt, Phys. Rev. D **68**, 114014 (2003).
[21] M. L. Mangano, M. Moretti, F. Piccinini, R. Pittau, and A. Polosa, J. High Energy Phys. 07 (2003) 001.
[22] F. Maltoni and T. Stelzer, J. High Energy Phys. 02 (2003) 027.
[23] E. Gerchtein and M. Paulini, Report No. CHEP-2003-TUMT005, 2003.
[24] H. L. Lai *et al.*, Eur. Phys. J. C **12**, 375 (2000).
[25] D. Scott, *Multivariate Density Estimation: Theory, Practice, and Visualization* (Wiley, New York, 1992).
[26] See, for example, the monographs W. P. Elderton and N. L. Johnson, *Systems of Frequency Curves* (Cambridge University Press, Cambridge, England, 1969); G. J. Hahn and S. S. Shapiro, *Statistical Models in Engineering* (Wiley, New York, 1967). To compute the Johnson functions, we use an algorithm described in I. D. Hill, R. Hill, and R. L. Holder, Appl. Statist. **25**, 180 (1976).
[27] This assumption is not true in general. The $\vec{x} \rightarrow \vec{x}_{\mathrm{eff}}$ mapping involves smearing due to hadronization and angular resolution, so the mapping is many-to-many. Our assumption produces just a first-order correction. However, the correction appears to be small, so we have stopped at this level.
[28] C. Peterson, T. Rögnvaldsson, and L. Lönnblad, Comput. Phys. Commun. **81**, 185 (1994).
[29] A. Abulencia *et al.* (CDF Collaboration), Phys. Rev. D **73**, 032003 (2006). Note that we use a procedure slightly different from the one described in this article; we use samples in which the ISR and FSR have been shifted together by a $\pm 1\sigma$ variation. The determination of the 1σ uncertainty is the same as described in this article.
[30] M. Bowler, Z. Phys. C **22**, 155 (1984).
[31] Y. Peters, K. Hamacher, and D. Wicke, FERMILAB Report No. Fermilab-TM-2425-E, 2009.
[32] D. Wicke and P. Z. Skands, arXiv:hep-ph/0807.3248.
[33] A. D. Martin, R. G. Roberts, W. J. Stirling, and R. S. Thorne, Eur. Phys. J. C **4**, 463 (1998).